The Astrophysical Journal, 1007:7 (22pp), 2026 August 10 https://doi.org/10.3847/1538-4357/ae819e

Photometric and Spectroscopic Studies of Type Ic Supernovae SN 2020akf and SN 2021mxx

Mulchand Kurre[1,10], K. R. Sahu[1,2], Shrutika Tiwari[3], Yogita Patel[4], N. K. Chakradhari[1,10], D. K. Sahu[5], Rishabh Singh Teja[6], G. C. Anupama[5], Mridweeka Singh[5], Anirban Dutta[7,8], and Anjasha Gangopadhyay[9]
[1] School of Studies in Physics and Astrophysics, Pt. Ravishankar Shukla University, Raipur 492010, India; mulkurre123@gmail.com, nkchakradhari@gmail.com
[2] Sant Guru Ghasidas Govt. Post Graduate College, Kurud, Dhamtari, 493663, India
[3] Faculty of Science, The ICFAI University, Raipur 490042, India
[4] Department of Astronomy, University of Chile, Santiago 7591245, Chile
[5] Indian Institute of Astrophysics, Koramangala II Block, Bengaluru 560034, India; dks@iiap.res.in
[6] Tsung-Dao Lee Institute, Shanghai Jiao Tong University, No.1 Lisuo Road, Pudong New Area, Shanghai, People's Republic of China
[7] Department of Physics and Astronomy, Michigan State University, East Lansing, MI 48824, USA
[8] Graduate Institute of Astronomy, National Central University, 300 Jhongda Road, 32001, Jhongli, Taiwan
[9] The Oskar Klein Centre, Department of Astronomy, Stockholm University, Albanova, 106 91 Stockholm, Sweden
Received 2025 December 16; revised 2026 June 10; accepted 2026 June 22; published 2026 July 31

Abstract

We present a comprehensive analysis of optical photometry and medium-resolution spectroscopy for Type Ic supernovae (SNe) SN 2020akf and SN 2021mxx. Our study covers the evolution of SN 2020akf from −5 to 109 days and SN 2021mxx from −3 to 115 days relative to their *B*-band maximum. Their peak quasi-bolometric luminosities are estimated at $\log L_{\rm bol}^{\rm max} = 42.37 \pm 0.02$ erg s^{-1} and 42.21 ± 0.02 erg s^{-1}, respectively. The velocities of ejecta, derived from the Fe II λ5169 line at maximum light, are approximately 15,000 km s^{-1} for SN 2020akf and about 10,000 km s^{-1} for SN 2021mxx, which are consistent with those observed in other Type Ic SNe. Using the semianalytical Arnett model, we estimate that SN 2020akf has a kinetic energy of $E_k = 6.33^{+0.68}_{-0.62} \times 10^{51}$ erg and an ejected mass of $M_{\rm ej} = 4.71^{+0.50}_{-0.46}$ $M_\odot$, while for SN 2021mxx we get $E_k = 0.54^{+0.08}_{-0.12} \times 10^{51}$ erg and $M_{\rm ej} = 0.90^{+0.14}_{-0.18}$ $M_\odot$. The mass of ^{56}Ni synthesized in the explosion is estimated at 0.10 ± 0.02 $M_\odot$ for SN 2020akf and 0.05 ± 0.01 $M_\odot$ for SN 2021mxx. The metallicities of the host galaxies near the SN regions are ∼0.81 $Z_\odot$ for SN 2020akf and ∼0.76 $Z_\odot$ for SN 2021mxx, where $Z_\odot$ indicates solar metallicity. Our detailed analysis suggests that SN 2020akf falls into the category of a transitional Type Ic SN, having spectral properties between normal and broad-line Type Ic SNe, while SN 2021mxx is a normal Type Ic SN with an extremely low value of the $M_{\rm ej}/E_k$ ratio.

Unified Astronomy Thesaurus concepts: Supernovae (1668); Type Ic supernovae (1730); Photometry (1234); Spectroscopy (1558)

1. Introduction

Type Ib/c supernovae (SNe) are a subclass of core-collapse SNe (CCSNe), which result from the catastrophic gravitational collapse of the stellar cores in stars with zero-age main-sequence (ZAMS) masses ⩾8 $M_\odot$ (S. J. Smartt 2009). Their progenitor stars are believed to have lost their outer envelopes owing to strong stellar winds in the case of single massive stars, such as Wolf–Rayet stars (S. C. Yoon et al. 2010; N. Smith et al. 2011; S.-C. Yoon 2015), or through interactions with a companion in binary systems (J. J. Eldridge et al. 2013). This stripping process results in the absence of lighter elements, such as hydrogen and helium, in their spectra. Together with the Type IIb subclass, these SNe are collectively called stripped-envelope (SE) CCSNe (A. Clocchiatti et al. 1996).

The presence or absence of He features, as well as their strength and evolution, are crucial to distinguish between Type Ib and Type Ic SNe. Type Ib SNe display prominent He I lines in their spectra, while Type Ic SNe are characterized by the absence of H and He lines (J. C. Wheeler & R. P. Harkness 1986; A. V. Filippenko et al. 1990; R. P. Harkness & J. C. Wheeler 1990; T. Matheson et al. 2001; L. H. Frey et al. 2013; Y.-Q. Liu et al. 2016). However, weak He lines have been detected in some Type Ic SNe, such as SN 1994I (M. Williamson et al. 2021), SN 2007gr (J. Chen et al. 2014), SN 2012ap (D. Milisavljevic et al. 2015), and SN 2016coi (M. Yamanaka et al. 2017; S. J. Prentice et al. 2018).

SESNe are characterized by diverse light-curve shapes, luminosities, and spectral features. Their light curves are mainly powered by the radioactive decay chain of ^{56}Ni, with the peak absolute magnitude ranging from $M_V = -16$ to −18.5 mag (F. Taddia et al. 2018). The expansion velocity of the ejecta is found to be (∼5000–25,000 km s^{-1}). A small fraction (∼4%) of Type Ic SNe (I. Shivvers et al. 2017) exhibit broad features corresponding to extremely high ejecta velocities ranging from ∼15,000 to 35,000 km s^{-1} and significantly higher kinetic energies ($E_k > 10^{52}$ erg), far exceeding that of typical SESNe. Such highly energetic events are referred to as "hypernovae" (K. Iwamoto et al. 1998), representing a subtype of Type Ic SNe known as broad-lined Type Ic (Ic-BL) SNe.

Type Ic-BL events are sometimes linked to long gamma-ray bursts (GRBs). The discovery of SN 1998bw associated with

[10] Centre for Mega Projects in Multiwavelength Astronomy, Pt. Ravishankar Shukla University, Raipur.

GRB 980425 (T. J. Galama et al. 1998), followed by several SN–GRB pairs (J. Hjorth et al. 2003; K. Z. Stanek et al. 2003; D. Malesani et al. 2004; E. Pian et al. 2006; F. Bufano et al. 2012; V. L. Toy et al. 2016), established a strong connection between some Type Ic-BL SNe and GRBs or X-ray flashes. However, late-time radio studies show that not all Ic-BL explosions are associated with GRBs (E. Berger et al. 2002; A. Corsi et al. 2011). In contrast, progenitors of normal Type Ic SNe are less extreme, most likely moderately massive Wolf–Rayet stars or interacting binaries. Extensive investigations into the progenitor pathways of Type Ibc SNe further support this picture (J. J. Eldridge et al. 2013; M. C. Bersten et al. 2014; J. J. Eldridge et al. 2015; H. Kuncarayakti et al. 2018; D. Vartanyan et al. 2021).

Over the past few decades, several distinct subclasses of SESNe have been discovered and investigated, including double-peaked Type Ib/c SNe (K. K. Das et al. 2024), Ca-rich transients (H. B. Perets et al. 2010; M. M. Kasliwal et al. 2012; S. Taubenberger 2017), and interacting SNe, such as Type Ibn (R. J. Foley et al. 2007; A. Pastorello et al. 2007; N. Smith et al. 2008) and Type Icn (M. Fraser et al. 2021; A. Gal-Yam et al. 2022; C. Pellegrino et al. 2022; D. A. Perley et al. 2022). The growing diversity of SESNe poses significant challenges to their study but also provides an opportunity to better understand their progenitor systems, explosion mechanisms, and environmental influences. Comprehensive, object-specific studies are therefore crucial in advancing our understanding of SESNe.

This paper presents a detailed optical photometric and spectroscopic analysis of two Type Ic events, SN 2020akf and SN 2021mxx. SN 2020akf was reported by the Asteroid Terrestrial-impact Last Alert System (ATLAS; J. L. Tonry et al. 2018) on 2020 January 20, with the internal name ATLAS20bmm (J. Tonry et al. 2020). It was located at R.A. = 09:28:39.6, decl. = +38:33:47.1, within the host galaxy KUG 0925+387B ($z = 0.012445 \pm 0.000011$; source: NASA/IPAC Extragalactic Database (NED), F. D. Albareti et al. 2017). SN 2021mxx was discovered on 2021 May 22 (F. Forster et al. 2021), by the Zwicky Transient Facility (ZTF; E. C. Bellm et al. 2019) at a magnitude of 17.45 in the ZTF-r band and was given the internal designation ZTF21abcgaln. The SN was located in the host galaxy UGC 11380 ($z = 0.009650 \pm 0.000060$; source: NED, L. Bottinelli et al. 1993) at R.A. = 18:56:51.3, decl. = +36:37:20.4. The identification charts for SN 2020akf and SN 2021mxx are displayed in Figure 1. Some important parameters of SN 2020akf, SN 2021mxx, and their host galaxies (KUG 0925+387B, UGC 11380) are given in Table 1 in the Appendix.

Initially, both SN 2020akf (J. Burke et al. 2020) and SN 2021mxx (C. Pellegrino et al. 2021) were classified as Type Ia SNe. However, SN 2021mxx was later reclassified as a Type Ic SN by A. Dahiwale and C. Fremling on behalf of ZTF.[11] Applying the Supernova Identification (SNID) code to near-maximum light spectra, M. Williamson et al. (2023) confirmed that both SNe are indeed Type Ic SNe.

This paper is organized as follows: Section 2 provides an overview of the photometric observations and data reduction techniques, followed by detailed discussions on the light curve, color curve, reddening, distance, and absolute magnitude. Section 2.4 outlines the evolution of the quasi-bolometric light curve. Section 3 focuses on spectroscopic observations, data analysis, and the evolution of the spectra and photospheric velocity. Section 4 presents the estimation of oxygen mass, and Section 5 examines the metallicity of the SN regions within the host galaxy. The key explosion parameters are derived in Section 6. Finally, Section 7 provides a discussion and summary of this work.

2. Photometric Studies

2.1. Observations and Data Reduction

The optical imaging of SN 2020akf and SN 2021mxx was performed in Bessell's *UBVRI* bands using the Himalaya Faint Object Spectrograph Camera (HFOSC), mounted on the 2 m Himalayan Chandra Telescope (HCT) at the Indian Astronomical Observatory (IAO), Hanle. The central 2K × 2K pixels of the 2K × 4K pixel SITe CCD chip are used for imaging observations. With a plate scale of $0\overset{''}{.}296$ pixel^{-1}, this provides a field of view of 10 × 10 arcmin^2. The CCD has a gain of 1.22 e$^-$/ADU and a readout noise of 4.87 e$^-$. More detailed information on the telescope and instrument can be found in T. P. Prabhu (2000) and at the IIA-IAO webpage.[12]

SN 2020akf was monitored from 2020 January 26 to May 19, while SN 2021mxx was monitored from 2021 May 25 to September 20. In addition to the SN frames, several calibration frames, including twilight flats and bias frames, were obtained.

The standard-star fields PG 0231+051, PG 0918+029, PG 0942–029, PG 1047+033, PG 1323–086, PG 1528+062, and PG 1633+099 from A. U. Landolt (2009) were observed on photometric nights during the observations of SN 2020akf on 2020 January 26, February 3, and April 16. Similarly, for SN 2021mxx, the standard-star fields PG 1633+099, PG 1657+078, PG 2213–006, and PG 1528+062 were observed on 2023 March 13. These standard fields were used to calibrate a set of secondary standards within the SN fields of SN 2020akf and SN 2021mxx, as marked in Figure 1.

Standard data processing steps, including bias subtraction and flat-field correction, were carried out using the Image Reduction and Analysis Facility (IRAF[13]) package.

Aperture photometry was performed on the Landolt standard stars. The photometric zero-points were calculated by taking the average atmospheric extinction for the IAO-Hanle site and the average color terms for the HFOSC. The sequence of secondary standards, calibrated using the calculated zero-points and average color terms, is listed in Table 2 in the Appendix.

SN 2020akf and SN 2021mxx both occurred near the nuclei of their respective host galaxies, in regions with high and variable background levels. To reduce the host galaxy's contribution to the SN flux, a template-subtraction method was used. Deep *UBVRI* template images of the KUG 0925+387B and UGC 11380 fields were obtained using the same instrumental setup once the SNe faded sufficiently below the detection threshold. These template images were subtracted from the individual SN frames following a standard procedure. Aperture photometry was then performed on the SN left in the template-subtracted frames, which was differentially calibrated relative to secondary standard stars. The final magnitudes of

[11] https://www.wis-tns.org/object/2021mxx

[12] http://www.iiap.res.in/centers/iao

[13] https://iraf-community.github.io/

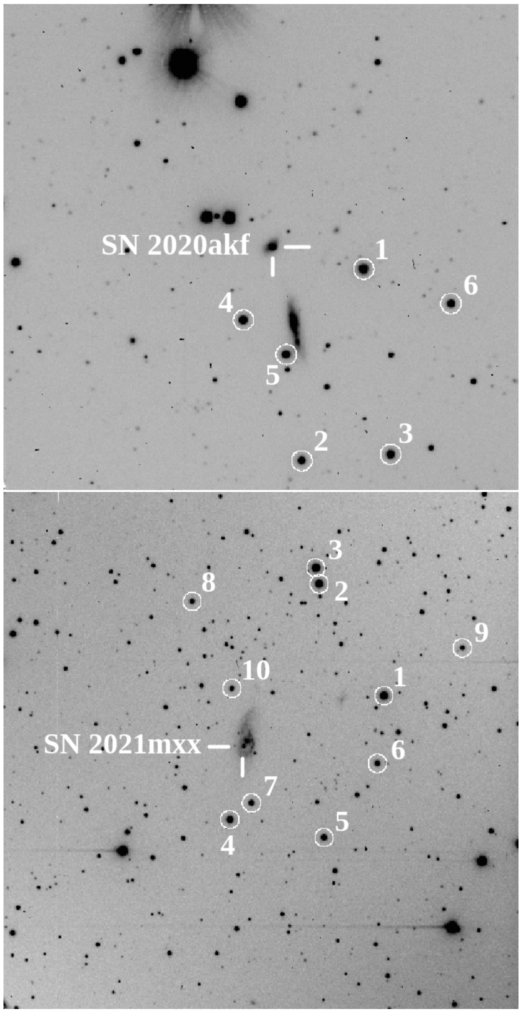

Figure 1. Identification charts, with north oriented upward and east to the left, for SN 2020akf (top) and SN 2021mxx (bottom). Stars marked were used as secondary standards.

SN 2020akf and SN 2021mxx are provided in Tables 3 and 4, respectively, in the Appendix.

For this study, we also utilized photometric data in the *g* and *r* bands from AleRCE/ZTF (E. C. Bellm et al. 2019) and the *c*-cyan and *o*-orange bands from the ATLAS forced photometry (J. L. Tonry et al. 2018; K. W. Smith et al. 2020) database. ZTF photometry is performed using the ZTF pipeline (F. J. Masci et al. 2019, 2023), which employs difference-imaging analysis, and calibrated to the ZTF system using Pan-STARRS1 reference stars. The ATLAS *c*- and *o*-band photometric measurements are derived from difference images with host galaxy subtraction applied and are calibrated to the ATLAS photometric system, accounting for filter-detector response (J. L. Tonry et al. 2018).

2.2. Light-curve and Color-curve Evolution

The optical light curves of SN 2020akf are shown in the top panel of Figure 2. The prediscovery limiting magnitude in the ATLAS *o* band and the discovery magnitude in the *c* band are indicated. Similarly, the *UBVRI*-band light curves of SN 2021mxx, along with the data points in the *c* and *o* bands from ATLAS and the *g* and *r* bands from ZTF, are displayed in the bottom panel of Figure 2. The prediscovery nondetection limits in the *g* and *r* bands are also shown.

The date of maximum brightness in the *UBVRI* bands for each SN was estimated by iteratively fitting a cubic spline to the observed data points around peak brightness. The estimated values are given in Table 5 in the Appendix. For SN 2020akf, the *B* band reached its maximum brightness on JD $2,458,880.4 \pm 0.5$ with an apparent magnitude of 16.34 ± 0.02 mag. The *U* band peaked $\sim$2 days before, while the *V* band peaked around 6 days after and the *R* and *I* bands peaked $\sim$9 days after the *B*-band maximum. For SN 2021mxx, the *B* band reached its peak on JD $2,459,363.3 \pm 0.5$, with an apparent magnitude of 16.90 ± 0.03 mag. The *U* band peaked $\sim$0.5 days earlier. The *V*-band peak occurred $\sim$2 days after and the *R*- and *I*-band peaks occurred $\sim$3.5 days after the *B*-band maximum.

SN 2020akf was discovered on 2020 January 20, at 12:04:19 UTC (JD 2,458,869.0), with an apparent magnitude of 18.89 mag. Its last nondetection was on 2020 January 18, at 12:43:12 UTC (JD 2458867.0), with a limiting magnitude of 19.64 mag (J. Tonry et al. 2020). We estimated the explosion epoch to be $\mathrm{JD_{exp}} = 245\,8864.46^{+0.28}_{-0.30}$ for SN 2020akf and $\mathrm{JD_{exp}} = 245\,9352.86^{+0.74}_{-0.57}$ days for SN 2021mxx (refer to Section 6.1). The observed time of maximum brightness suggests that SN 2020akf reached peak brightness with a rise time of $t_r \sim 16 \pm 1$ days in the *B* band, $t_r \sim 22 \pm 1$ days in the *V* band, and $t_r \sim 24.5 \pm 1$ days in the *R* band. For SN 2021mxx, the rise time was $\sim 10.44 \pm 1$ days, 12.2 ± 1 days, and 14 ± 1 days in the *B*, *V*, and *R* bands, respectively. SN 2021mxx reached peak brightness faster than SN 2020akf in all bands.

The post-peak light-curve evolution of both SNe shows a rapid decline in the *U* and *B* bands, while the *V*-, *R*-, and *I*-band light curves exhibit a slower decline. In the *B* band, the decline in magnitude 15 days after peak brightness, represented by the $\Delta m_{15}(B)$ parameter, is estimated as 0.98 ± 0.02 for SN 2020akf and 1.52 ± 0.03 for SN 2021mxx. The declines in the other bands are listed in Table 5 in the Appendix.

The *UBVRI* light curves of SN 2020akf and SN 2021mxx are compared in Figure 3 with those of several well-studied Type Ic SNe, including SN 1994I (M. W. Richmond et al. 1996), SN 2007gr (J. Chen et al. 2014), SN 2014L (J. Zhang et al. 2018), narrow-line Type Ic event SN 2017ein (D. Xiang et al. 2019), intermediate Type Ic event SN 2004aw (S. Taubenberger et al. 2006), and Type Ic-BL events SN 2002ap (R. J. Foley et al. 2003), SN 2007ru (D. K. Sahu et al. 2009), SN 2012ap (D. Milisavljevic et al. 2015), SN 2014ad (D. K. Sahu et al. 2018), and GRB 980425/SN 1998bw (T. J. Galama et al. 1998).

The early phase light curves of SN 2020akf, SN 2021mxx, and other SNe appear similar in the *U* band, while in the *BVRI* bands the light curves of SN 2020akf are broader than those of SN 2021mxx. The light curves of SN 2020akf match well with the broad light curves of SN 2004aw, with a similar rise time. In contrast, the light curves and the rise to maximum of SN 2021mxx match well with those of SN 2007gr, SN 2012ap, and SN 2014L (see also Figure 5).

The reddening-corrected color curves of SN 2020akf and SN 2021mxx are displayed in Figure 4, alongside those of other Type Ic SNe. The corrections for color excess were applied using $E(B-V) = 0.013$ mag for SN 2020akf and

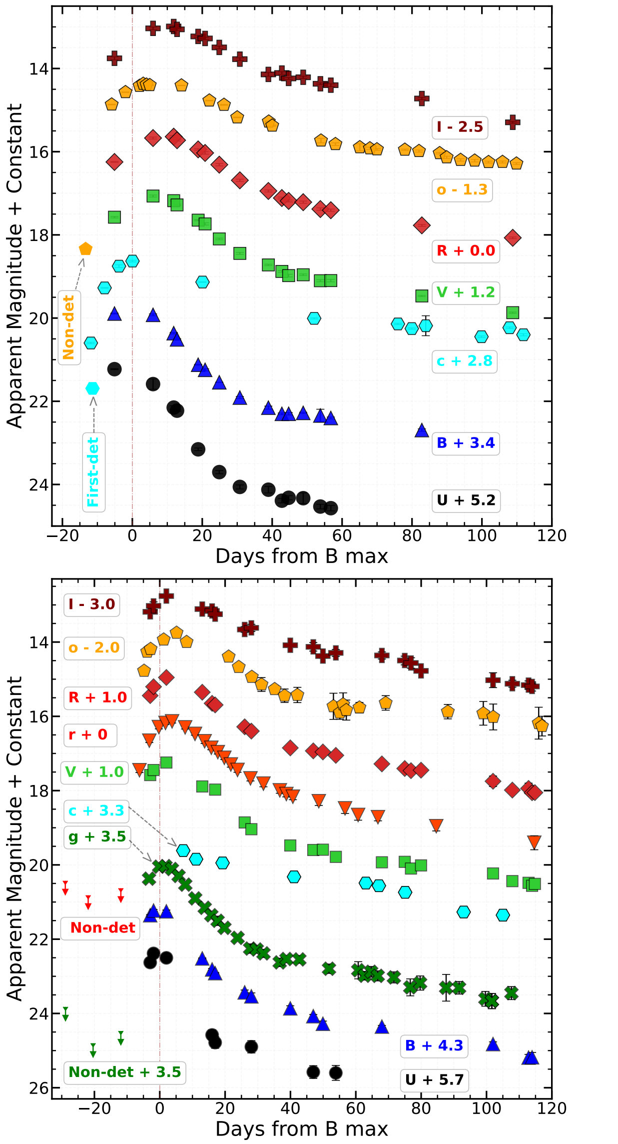

Figure 2. The multiband light curves of SN 2020akf (top) and SN 2021mxx (bottom). Each light curve is vertically shifted by the amount indicated in the legend for clarity. Phases are measured in days from the *B*-band maximum, marked by a vertical line in each panel. The prediscovery nondetection limits for SN 2021mxx in the ZTF *g* and *r* bands, binned at ∼10 days, are also shown.

$E(B-V)=0.20$ mag for SN 2021mxx (refer to Section 2.3). The $E(B-V)$ values for other SNe were obtained from their respective references.

The early $(U-B)$ color evolution of both SN 2020akf and SN 2021mxx is similar and aligns well with most of the Type Ic SNe used for comparison, except for SN 2002ap and SN 2007gr. However, in later stages, SN 2021mxx becomes bluer. The $(B-V)$, $(V-R)$, and $(R-I)$ colors of both SN 2020akf and SN 2021mxx also exhibit similarities to those of most other Type Ic SNe.

2.3. Reddening, Distance, and Absolute Magnitudes

To estimate the Galactic reddening in the direction of SN 2020akf and SN 2021mxx, we used the infrared dust map (E. F. Schlafly & D. P. Finkbeiner 2011). The derived values of $E(B-V)_{\rm Gal}$ for SN 2020akf and SN 2021mxx are

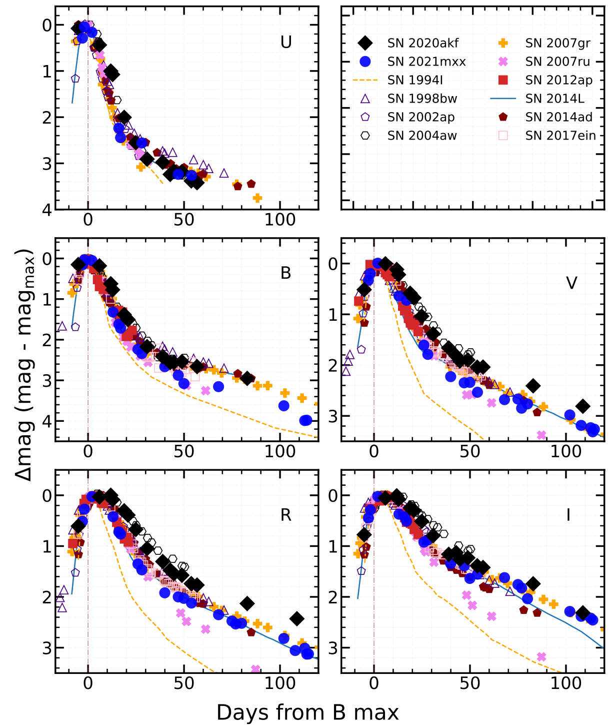

Figure 3. Comparison of the *UBVRI* light curves of SN 2020akf and SN 2021mxx with those of other well-studied Type Ic SNe. The light curves are shifted to align with their peak brightness and the epoch of the *B*-band maximum.

0.013 ± 0.001 mag and 0.08 ± 0.002 mag, respectively. Medium-resolution spectra of SN 2020akf and SN 2021mxx, taken around the epoch of maximum light, do not show the Na I D absorption line from interstellar matter within the Milky Way or the host galaxies.

M. D. Stritzinger et al. (2018) have analyzed the color evolution of a sample of SESNe from the Carnegie Supernova Project (CSP). They showed that the color evolution of the minimally reddened subsample reveals a high degree of homogeneity during 0 to +20 days with respect to the *B*-band maximum. The $(B-V)$ color curves of SN 2020akf and SN 2021mxx, corrected for Galactic reddening, were compared with the color template of M. D. Stritzinger et al. (2018) in Figure 4 to estimate host reddening. The color curve of SN 2020akf matches well with the template; hence, Galactic reddening is taken as the total reddening for this event. For SN 2021mxx, a vertical shift of 0.12 mag was required to match the template, giving $E(B-V)_{\rm total} = 0.20$ mag. For comparison, we have also plotted the color evolution of some well-studied Type Ic SNe in Figure 4.

To estimate the distances to the host galaxies KUG 0925+387B (for SN 2020akf) and UGC 11380 (for SN 2021mxx), we used the radial velocities of the hosts, corrected for Local Group infall onto the Virgo Cluster. The corrected velocities are $v = 3903 \pm 14$ km s^{-1} for KUG 0925+387B and $v = 3225 \pm 25$ km s^{-1} for UGC 11380 (source: NED, J. R. Mould et al. 2000). Adopting a value of $H_0 = 72 \pm 5$ km s^{-1} Mpc^{-1} (W. L. Freedman et al. 2001), we estimated the distance to SN 2020akf to be 54.21 ± 4 Mpc, corresponding to a distance modulus of 33.67 ± 0.15 mag. For SN 2021mxx, the estimated distance is 44.79 ± 3 Mpc, with a distance modulus of 33.26 ± 0.15 mag.

The peak absolute magnitudes of SN 2020akf and SN 2021mxx in various bands were estimated using the calculated

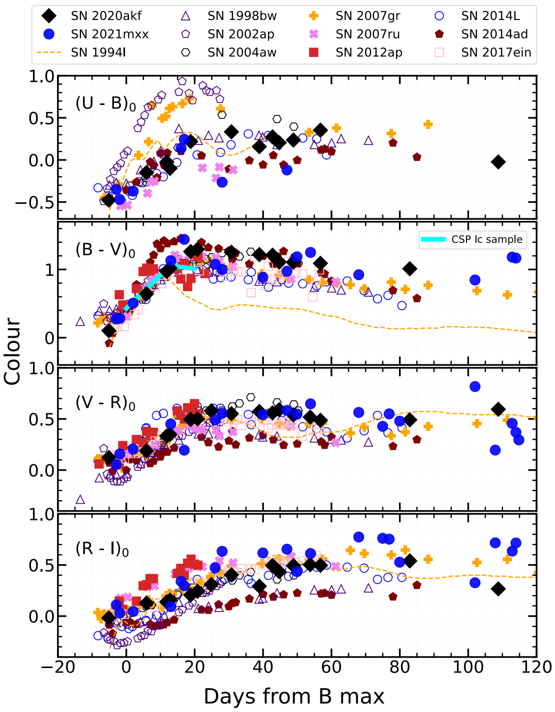

Figure 4. The reddening-corrected $(U-B)$, $(B-V)$, $(V-R)$, and $(R-I)$ color curves of SN 2020akf and SN 2021mxx are compared with those of other well-studied Type Ic SNe. The $(B-V)$ color evolution of the minimally reddened sample of Type Ic SNe from the CSP (M. D. Stritzinger et al. 2018) is also shown.

reddening values and distance moduli. The values are listed in Table 5 in the Appendix. The V-band peak absolute magnitudes are -17.85 ± 0.15 mag for SN 2020akf and -17.60 ± 0.15 mag for SN 2021mxx. SN 2020akf and SN 2021mxx are brighter than SN 2002ap ($M_V = -17.37 \pm 0.05$ mag; R. J. Foley et al. 2003; S. B. Pandey et al. 2003), SN 2007gr ($M_V = -17.22 \pm 0.18$ mag; D. J. Hunter et al. 2009), and SN 2017ein ($M_V = -17.47 \pm 0.35$ mag; D. Xiang et al. 2019). Their absolute magnitude is comparable to that of SN 1994I ($M_V = -17.62 \pm 0.3$ mag; M. W. Richmond et al. 1996; D. N. Sauer et al. 2006) and SN 2014L ($M_V = -17.73 \pm 0.28$ mag; J. Zhang et al. 2018) but lower than that of SN 2004aw ($M_V = -18.02 \pm 0.3$ mag; S. Taubenberger et al. 2006), SN 2012ap ($M_V = -18.67 \pm 0.08$ mag; D. Milisavljevic et al. 2015), and SN 2014ad ($M_V = -18.86 \pm 0.23$ mag; D. K. Sahu et al. 2018).

2.4. Bolometric Luminosity

The quasi-bolometric light curves of SN 2020akf and SN 2021mxx were estimated from the *U BV RoI* and *U Bg Vr RI* observations described in Section 2. The magnitudes were corrected for reddening, with $E(B-V)$ values of 0.013 and 0.20 mag, respectively, following the J. A. Cardelli et al. (1989) extinction law. Using the distances derived in Section 2.3, these corrected magnitudes were used to construct the bolometric light curves with the SuperBol code (M. Nicholl 2018).

A well-sampled light curve is first selected as the reference band. The remaining bands are then interpolated and, when necessary, extrapolated to match the temporal coverage of this reference. Interpolation is performed iteratively using polynomial fits (typically third order), with visual inspection at each step to ensure a satisfactory representation of the

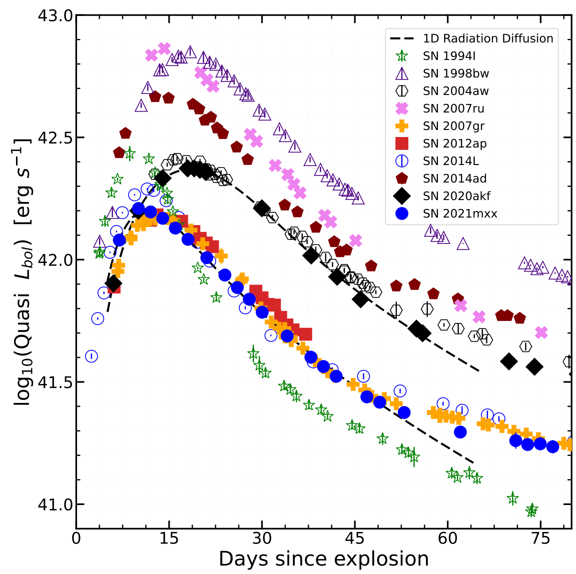

Figure 5. The quasi-bolometric light curves of SN 2020akf (*U BV RoI*) and SN 2021mxx (*U BgV r RI*) are compared with the quasi-bolometric (*U BV RI*) light curves of other Type Ic SNe, all derived using the SuperBol code (M. Nicholl 2018). The dashed lines represent the Arnett–Valenti model fit (Section 6.1) to the quasi-bolometric light curves of SN 2020akf and SN 2021mxx.

observed data. Extrapolation is applied only when required to align the boundary epochs. In such cases, a constant color offset relative to the reference band is assumed, determined from the nearest available data points. To minimize extrapolation, we limited the data to epochs within ∼75 days of the B-band maximum. The resulting light curves were then used to construct the quasi-bolometric light curves.

The quasi-bolometric light curves of SN 2020akf and SN 2021mxx are shown in Figure 5. The peak quasi-bolometric luminosities were estimated to be $(2.36 \pm 0.11) \times 10^{42}$ erg s^{-1} for SN 2020akf and $(1.62 \pm 0.08) \times 10^{42}$ erg s^{-1} for SN 2021mxx.

Based on the study by S. J. Prentice et al. (2016), we included the near-infrared (NIR) and ultraviolet (UV) contributions to the *U BV RI* luminosity for Type Ib/c SNe, adopting typical values of ∼15% for the NIR and ∼10% for the UV contributions at peak brightness. The total peak bolometric luminosities were estimated to be $L_{\rm UVOIR} = (2.95 \pm 0.13) \times 10^{42}$ erg s^{-1} for SN 2020akf and $L_{\rm UVOIR} = (2.02 \pm 0.09) \times 10^{42}$ erg s^{-1} for SN 2021mxx.

The quasi-bolometric light curves of SN 2020akf and SN 2021mxx are compared with those of other well-studied Type Ic SNe in Figure 5. The quasi-bolometric light curve of SN 2020akf resembles that of SN 2004aw, whereas the light curve of SN 2021mxx is similar to those of SN 2007gr and SN 2012ap. Both SN 2020akf and SN 2021mxx exhibit significantly lower quasi-bolometric luminosities than Type Ic-BL SNe, such as SN 1998bw, SN 2007ru, and SN 2014ad. The early post-maximum decline, ΔM_{15}, of the quasi-bolometric magnitude light curves was approximately 0.57 mag for SN 2020akf and 0.77 mag for SN 2021mxx. During the late phase, decline rates were found to be 1.40 mag (100 days)$^{-1}$ for SN 2020akf and 1.61 mag (100 days)$^{-1}$ for SN 2021mxx. The decline of the quasi-bolometric light curve of both SNe in the

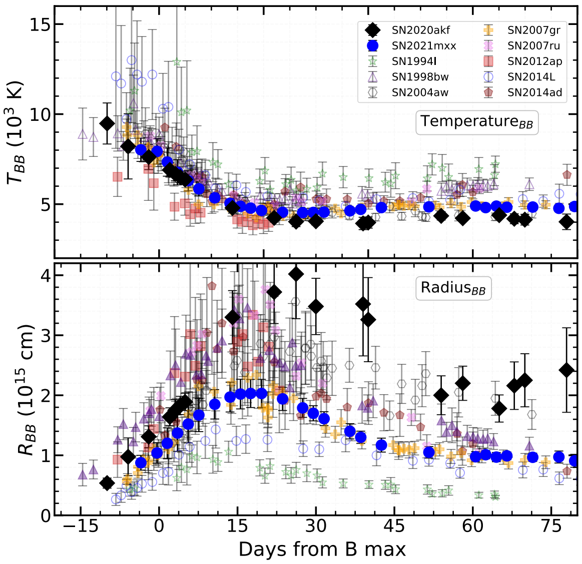

Figure 6. Photospheric temperature and radius evolution of SN 2020akf and SN 2021mxx, along with other Type Ic SNe derived using the SuperBol Code (M. Nicholl 2018).

late phase is significantly steeper than the decay rate of ^{56}Co to ^{56}Fe, indicating substantial gamma-ray leakage through the ejecta.

Figure 6 displays the blackbody temperature and radius evolution for both SNe, as inferred from SuperBol. While the temperature evolution is remarkably similar for both events, SN 2020akf exhibits a larger photospheric radius at peak brightness and in the later phases. As a result, SN 2020akf attains a higher luminosity compared to SN 2021mxx.

3. Spectroscopic Studies

3.1. Spectroscopic Observations and Data Reduction

Optical spectra for SN 2020akf and SN 2021mxx were obtained using HFOSC mounted on HCT. We employed Gr7 (wavelength range 3800–7000 Å) and Gr8 (5200–9200 Å) grisms, with a resolution of approximately 7 Å. Detailed information about spectroscopic observations is provided in Table 6 in the Appendix. Our spectroscopic coverage spans from ∼−5 to +57 days for SN 2020akf and from ∼−3 to +113 days for SN 2021mxx, with respect to B-maximum.

The spectroscopic data were processed in a standard manner using various tasks available in IRAF. A one-dimensional spectrum was extracted using the optimal extraction method. Dispersion solution and wavelength calibration were achieved using FeAr and FeNe arc lamp spectra. The wavelength calibration accuracy was validated by comparing it against night-sky emission lines, with minor adjustments applied as needed. We preferably used spectrophotometric standard stars observed on the same night to correct for the instrumental response and perform flux calibration. In the absence of a spectrophotometric standard star observed on the same night, observations from adjacent nights were utilized. The spectra from the blue and red regions (Gr7 and Gr8) were combined and scaled to a weighted mean, resulting in the final spectrum on a relative flux scale. The combined spectra were finally scaled with respect to the photometric flux to bring them to an absolute flux scale.

We applied reddening corrections in the spectra, with $E(B-V)_{\rm total} = 0.013$ mag for SN 2020akf and $E(B-V)_{\rm total} = 0.20$ mag for SN 2021mxx. The spectra of SN 2020akf and SN 2021mxx were corrected for the redshift of their host galaxies, using values of $z = 0.012445$ and $z = 0.000965$, respectively, as obtained from NED.

3.2. Spectral Evolution in Pre-maximum Phase

Spectral evolution of SN 2020akf (top) and SN 2021mxx (bottom) during the pre-maximum phase is shown in Figure 7, along with spectra of other Type Ic SNe, including SN 1994I, SN 2004aw, SN 2005mf, SN 2007gr, SN 2007ru and SN 2017ein, at comparable epochs, available publicly on WISeREP[14] (O. Yaron & A. Gal-Yam 2012). The spectrum of SN 2020akf in the pre-maximum phase was obtained at −5 days, while pre-maximum spectra of SN 2021mxx were obtained at −3 and −2 days relative to the B-band maximum. To investigate the early characteristics, we made use of pre-maximum spectra of SN 2020akf at −9 days (J. Burke et al. 2020) and SN 2021mxx at −5 days (C. Pellegrino et al. 2021) from WISeREP/TNS, included in Figure 7.

Both SN 2020akf and SN 2021mxx exhibit a blue continuum with prominent absorption features near ∼3800 and ∼4400 Å, attributed to Ca II (H and K) and Mg II, respectively. Spectra of both SNe show a blend of Fe II lines at approximately 4900 Å. The presence of the Si II λ6355 line around ∼6150 Å and the Ca II line near ∼8200 Å is clearly identifiable in the pre-maximum spectra of SN 2021mxx, whereas the Ca II line in SN 2020akf is still developing. The spectra of both SN 2020akf and SN 2021mxx show C II lines near ∼6300 Å; this feature is notably strong in SN 2020akf at −9 days but weakens significantly in later phases. A similar feature is observed in the spectra of SN 2007gr (J. Chen et al. 2014) and SN 2004aw. Overall, the spectral features of SN 2020akf and SN 2021mxx are consistent with those of other Type Ic SNe.

3.3. Spectral Evolution in Post-maximum Phase

The post-maximum spectral evolution of SN 2020akf (top panel) and SN 2021mxx (bottom panel) is presented in Figure 8. Up to ∼57 days, the evolution of SN 2020akf reveals the distinctive "W" feature of the Mg II (∼4400 Å) line, along with Fe II (∼4745 Å) and Fe II (∼4960 Å) lines. The evolution of the Na I line is also apparent. The Mg II and Si II lines gradually fade, and another "W" feature of the Fe II lines (∼5900 Å) begins to emerge around 25–40 days after maximum light. The Ca II NIR triplet's transition from an absorption to an emission feature occurs ∼25 days after maximum light.

In the spectral evolution of SN 2021mxx (Figure 8, bottom panel), the spectrum at 13 days shows the Fe II (∼4745 Å) and Fe II (∼4960 Å) lines, along with the Mg II (∼4400 Å) line, all of which are clearly developed. However, the Na I lines continue to evolve and become prominent after ∼17 days from maximum light. The Mg II and Si II λ6355 lines gradually weaken and begin to merge into the characteristic "W" feature of Fe II. The Ca II NIR absorption feature also evolves significantly, eventually becoming emission dominated.

Figure 9 shows the spectra of SN 2020akf and SN 2021mxx obtained at approximately ∼13 days (top panel) and 25 days

[14] https://www.wiserep.org/

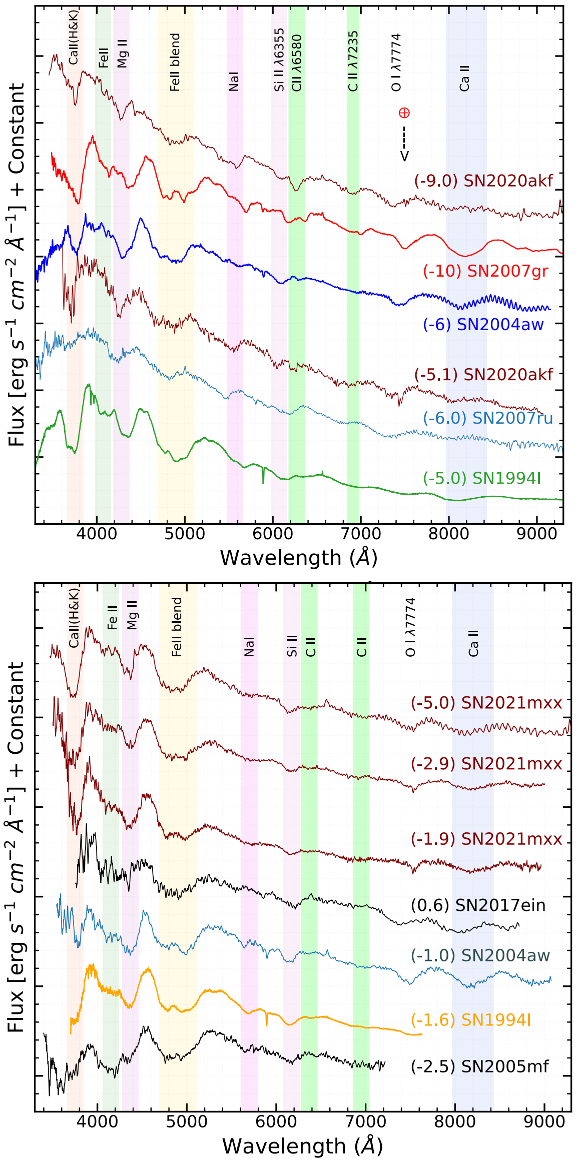

Figure 7. Pre-maximum spectral evolutions of SN 2020akf (top) and SN 2021mxx (bottom) compared with those of other well-studied Type Ic SNe. The prominent features in the spectra are marked. To enhance clarity, the spectra have been vertically shifted. Telluric lines are indicated by a circled plus sign.

(bottom panel), respectively, alongside other Type Ic SNe at similar epochs for comparison. In SN 2020akf, the "W" features of Fe II (∼4745 Å) and Fe II (∼4960 Å), as well as the Na I lines, resemble those seen in other SNe, including SN 1994I, SN 2014L, and SN 2017ein. The central portion of the SN 2020akf spectrum appears somewhat bumpy, a feature shared with SNe such as SN 2002ap, SN 2004aw, SN 2012ap, and SN 2017ein.

In SN 2021mxx, the blended Fe II lines are comparable to those in SN 2002ap, SN 2004aw, and SN 2012ap. However, the overall shape of SN 2021mxx's spectrum is flat, resembling those of SN 1994I and SN 2014L.

3.4. Spectral Evolution in Nebular Phase

Figure 10 presents the nebular-phase spectra of SN 2021mxx, obtained around 102 and 113 days, compared with nebular spectra of other Type Ic SNe. These spectra are dominated by [O I] λλ6300, 6363 and [Ca II] λλ7291, 7324 emission lines. The [Ca II] λλ7291, 7324 lines are blended with [Fe II] λλ7155, 7175, 7388, and 7452 and with [O II] λλ7320, 7330 forbidden emission lines (M. Stritzinger et al. 2009). The spectra also display a prominent Ca II NIR triplet emission line. The narrow Hα emission line from the host galaxy is clearly identifiable.

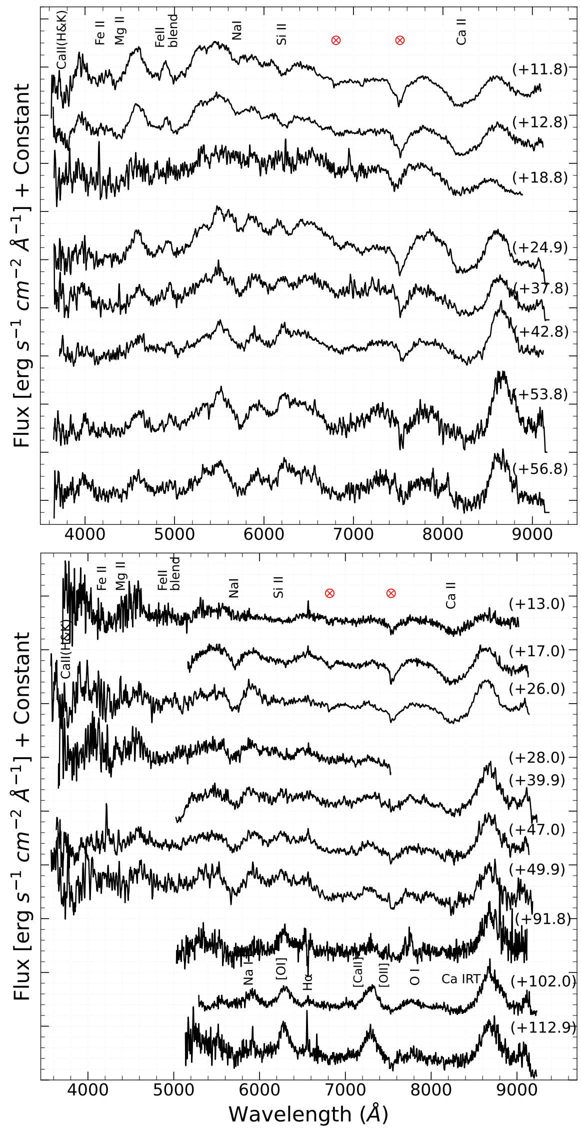

Figure 8. Spectral evolution of SN 2020akf (top panel) from ∼+12 to +57 days and for SN 2021mxx (bottom panel) from +13 to +113 days. To enhance clarity, the spectra have been vertically shifted. Telluric lines are indicated by a circled plus sign.

The nebular-phase spectra of SN 2021mxx are compared with those of Type Ic SNe SN 2007gr, SN 2014L, SN 2004aw, broad-lined SN 2002ap, and SN 1998bw around similar epochs. Prominent emission lines in SN 2021mxx, such as [O I] λλ6300, 6363, [Ca II] λλ7291, 7324, and the Ca II NIR triplet, appear similar to those in other SNe. The [Ca II] λλ7291, 7324 lines in SN 2021mxx and other typical Type Ic SNe are sharper, whereas they appear broad with a flat top in broad-lined Ic SN 1998bw and SN 2002ap. This broadening is attributed to blending of the [Ca II] λλ7291, 7324 lines with [Fe II], [O II], and [Co II] lines (K. Maeda et al. 2006, see their Figure 1).

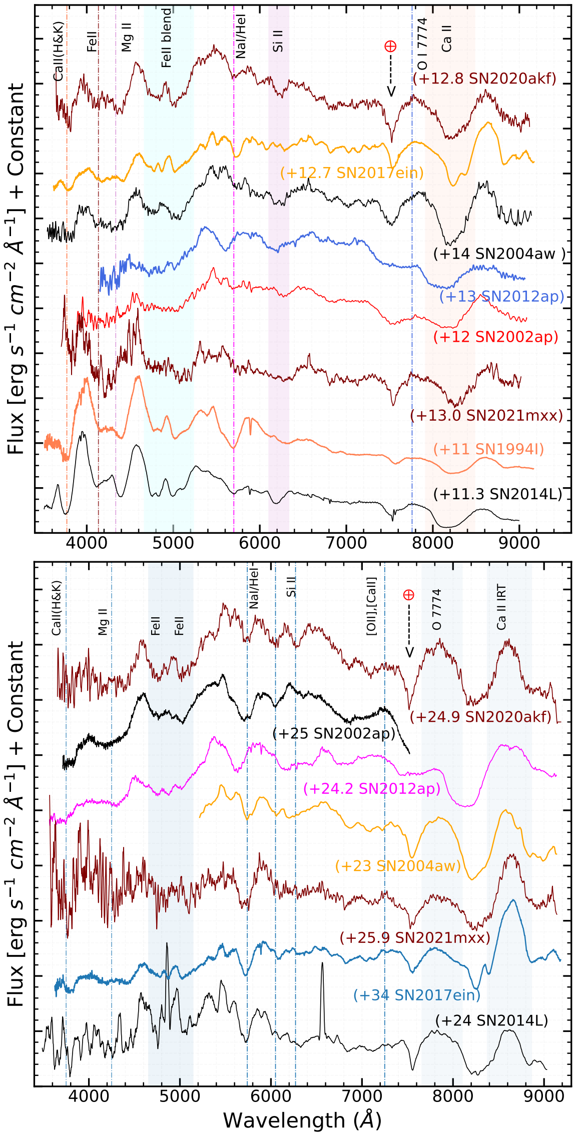

Figure 9. Comparison of spectra of SN 2020akf and SN 2021mxx at ∼13 days (top panel) and ∼25 days (bottom panel) with those of other Type Ic SNe at similar epochs. The prominent features in the spectra are marked. Telluric lines are indicated by a circled plus sign.

We used the `splot` task in IRAF to derive line-profile characteristics, e.g., line widths and line fluxes. For each emission feature, a local continuum was defined and subtracted, and the profile was fitted with a Gaussian function. The FWHM was derived from the fitted width and converted to velocity using the Doppler relation. Uncertainties were estimated by repeating the fits with reasonable variations in continuum placement and fitting regions. The line flux was obtained by integrating the best-fitting Gaussian profile.

The full width at half-maximum (FWHM) velocities for [O I] $\lambda\lambda$6300, 6363 in the spectra of SN 2021mxx at 102 and 113 days are approximately 9150 ± 550 and 6150 ± 535 km s^{-1}, respectively. Similarly, the FWHM velocities for [Ca II] $\lambda\lambda$7291, 7324 are around 7615 ± 500 km s^{-1} and 7100 ± 590 km s^{-1}, respectively. The FWHM velocities of these lines are higher than the core velocity values of 1000–5000 km s^{-1} suggested by C. Fransson & R. A. Chevalier (1989) depending on the envelope mass and the explosion energy. The higher core velocity may result from a more energetic explosion, significant mass loss

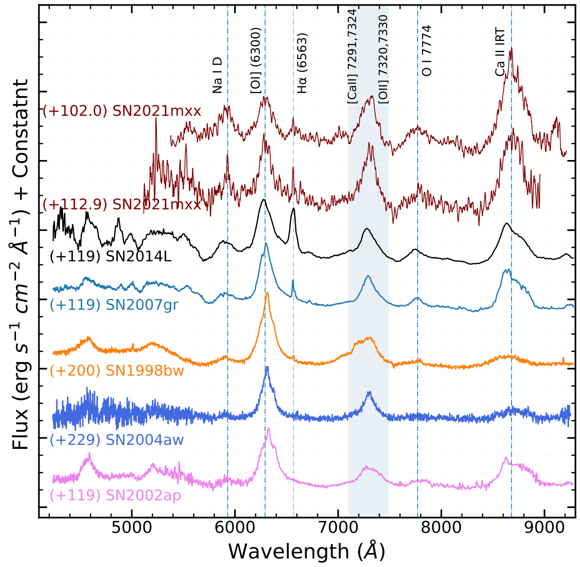

Figure 10. Nebular-phase spectra of SN 2021mxx at +102 and +113 days compared with those of other Type Ic SNe at similar epochs. The prominent features in the spectra are marked.

before the explosion, and mixing of the ejecta. This mixing can result in broader emission line profiles. Additionally, high core velocities could be associated with hydrodynamic instabilities, such as Rayleigh–Taylor instabilities, which would further influence the density distribution (C. Fransson & R. A. Chevalier 1989; A. V. Filippenko & W. L. W. Sargent 1985).

The line ratio of [O I] $\lambda\lambda$6300, 6363 to [Ca II] $\lambda\lambda$7291, 7324 is a good indicator for ZAMS mass of a progenitor star (K. Nomoto et al. 2006), and known to be insensitive to both density and temperature but increases with progenitor mass (C. Fransson & R. A. Chevalier 1989; A. Elmhamdi et al. 2004). For SN 2021mxx, the [O I]/[Ca II] line ratio is approximately 0.96, similar to that of SN 2012ap (0.9) and slightly more than that of SN 2009bb (0.8). However, it is notably lower than those of other Type Ic SNe, such as SN 2007gr (1.4), SN 2014L (1.5), and Type Ic-BL SNe like SN 1998bw (1.7), SN 2002ap (2), SN 2007ru (1.6), and SN 2014ad (1.54).

H. Kuncarayakti et al. (2015) investigated the [O I]/[Ca II] flux ratio in several CCSNe and linked it to progenitor properties. For SN 2021mxx, the measured flux ratio of 0.96 places it within the region associated with binary progenitors of Type Ib/c SNe. This suggests that SN 2021mxx likely originated from a lower-mass progenitor in a binary system.

A. Jerkstrand et al. (2015) have provided models for nebular spectra of Type IIb SNe, based on single-star evolutionary channels with progenitor masses of 12, 13, and 17 $M_\odot$. These model spectra depend on parameters such as the initial ^{56}Ni mass, distance, and time. The models assume a ^{56}Ni mass of 0.075 $M_\odot$ and a distance of 7.8 Mpc. In Figure 11 we compare the nebular-phase spectrum of SN 2021mxx with the models from A. Jerkstrand et al. (2015) at 100 days post-explosion. The observed spectrum of SN 2021mxx at 123 days post-explosion has been corrected for reddening and redshift and then scaled using Equation (2) from K. A. Bostroem et al. (2019), with a ^{56}Ni mass of 0.07 $M_\odot$ (estimated from complete bolometric luminosity), a distance of 44.79 Mpc, and the corresponding phase adjusted to match the model spectrum. A comparison of the nebular spectrum of SN 2021mxx with

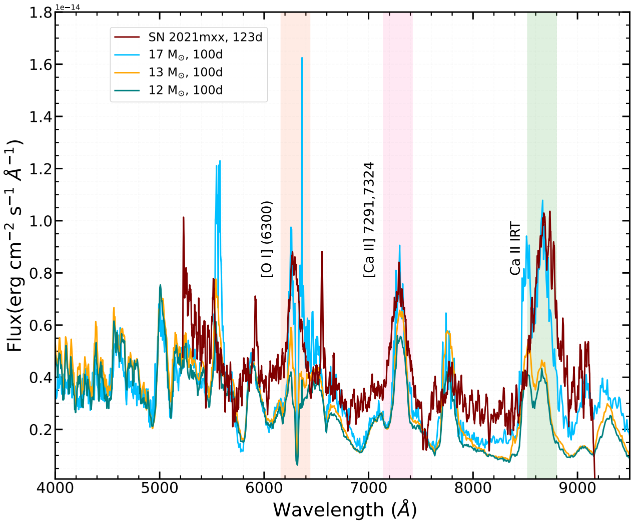

Figure 11. The nebular-phase spectrum of SN 2021mxx, observed 123 days post-explosion, compared with the models of A. Jerkstrand et al. (2015) for different progenitor masses.

various models indicates that its [O I] luminosity falls within the range predicted for progenitor masses of 13–17 $M_{\odot}$. Similar analyses have been performed for Type Ibc SNe by C. Fremling et al. (2016), A. Gangopadhyay et al. (2020), and M. Singh et al. (2021).

However, binary interaction prior to explosion can substantially modify the core structure and lower the final core progenitor mass of SESNe (M. C. Bersten et al. 2014; C. Fremling et al. 2016). Consequently, comparisons with single-star nebular models may systematically underestimate the ZAMS progenitor mass in systems that have experienced binary stripping. The mass estimates presented here should thus be regarded as lower limits.

3.5. Spectral Modeling with TARDIS

We use the one-dimensional radiative transfer code TARDIS[15] (W. E. Kerzendorf & S. A. Sim 2014; C. Vogl et al. 2019) to model the spectra and explore the physical conditions of the ejecta, including density structure, chemical composition, ionization state, and temperature distribution, for SN 2020akf and SN 2021mxx. Our modeling approach follows a configuration similar to those of L. A. Kwok et al. (2022) and M. Williamson et al. (2023), utilizing publicly available setup files.[16] We select a power-law density profile following homologous expansion with

$$\rho(v, t_{\rm exp}) = \rho_0 \left(\frac{v}{v_0}\right)^{-\alpha} \left(\frac{t_0}{t_{\rm exp}}\right)^3, \tag{1}$$

where ρ_0 is the inner density at the reference time t_0, v_0 is the reference velocity that governs the density slope, v is the photospheric velocity, $t_{\rm exp}$ is the time since explosion, and α is the power-law index. We used $\alpha = 6$, 30 iterations, and 300,000 packets for our analysis.

We assume a uniform fractional elemental abundance and use very simple elemental configurations of Ca, Fe, Ni, Mg, Si, Na, O, and C for SN 2020akf and SN 2021mxx. Our adopted density and elemental abundance profiles, along with the enclosed mass, that best fit the observed spectra are shown in Figure 12.

The model-fitting process was performed using the chi-by-eye method, similar to that described in B. Barna et al. (2021), L. A. Kwok et al. (2022), and M. Singh et al. (2024). The best-fit parameters are $\rho_0 = 8.5 \times 10^{-16}$ g cm^{-3}, $t_0 = 16$ days, and $v_0 = 20{,}000$ km s^{-1} for SN 2020akf and $\rho_0 = 1.0 \times 10^{-14}$ g cm^{-3}, $t_0 = 10$ days, and $v_0 = 15{,}000$ km s^{-1} for SN 2021mxx. These best-fit parameters were fixed and used consistently to model the spectra at three epochs for each SN, successfully reproducing the key spectral features of SN 2020akf at −5, +12, and +13 days (left column) and SN 2021mxx at −3, −2, and +13 days (right column) as shown in Figure 13.

To estimate the enclosed mass within the velocity range $v_{\rm min}$ and $v_{\rm max}$ for SN 2020akf at −5 days, the TARDIS model density profile was integrated between 12,000 and 30,000 km s^{-1}. A similar exercise was done for SN 2021mxx at −3 days within the velocity range 10,000–30,000 km s^{-1}. The total enclosed mass was computed within 30 discrete velocity shells. The resulting velocity-dependent enclosed mass distributions for both SNe are shown in Figure 12. SN 2020akf has a higher density than SN 2021mxx, resulting in a greater ejecta mass.

We examined the convergence of our TARDIS model by tracking the evolution of the radiation temperature ($T_{\rm rad}$) and dilution factor (W) across 30 iterations, for SN 2020akf and SN 2021mxx. The deviation in iteration is minimal after the third iteration, and both parameters stabilize by reaching a velocity of ∼29,000 km s^{-1}. Beyond this point, the values vary negligibly with velocity throughout the iteration, indicating that the model has reached a stable solution. This trend was observed in both SNe. The convergence plots for the radiation temperature and dilution factor of SN 2020akf and SN 2021mxx are shown in Figure 18 in the Appendix.

3.6. Photospheric Expansion Velocity

In Type Ib/c SNe, Fe II lines near 5000 Å are often employed to estimate the photospheric expansion velocity of the ejecta. However, in the cases where the Fe II lines are blended, the Si II λ6355 line serves as a reliable alternative indicator for photospheric velocity.

For both SN 2020akf and SN 2021mxx, we estimated the expansion velocity of the ejecta using the Fe II λ5169, Si II λ6355, and Ca II NIR triplet lines by fitting a Gaussian profile to their absorption trough in the redshift-corrected spectra, as presented in Figure 14 (top panel). The velocity estimated using the Ca II NIR triplet and Fe II is found to be higher than the Si II line velocity, as seen in other Type Ic SNe. For SN 2020akf, Ca II velocity declines from 22,500 ± 760 km s^{-1} at −9 days to 17,000 ± 525 km s^{-1} at +10 days. Similarly, for SN 2021mxx, the Ca II velocity declines from 16,500 ± 525 km s^{-1} at −5 days to 11,000 ± 590 km s^{-1} at +10 days. The higher velocity of the Ca II line indicates that calcium was distributed up to the outermost layers of the ejecta. The Fe II line velocity declines from 18,000 ± 570 km s^{-1} at −9 days to 10,000 ± 550 km s^{-1} at +20 days for SN 202akf. In SN 2021mxx, the Fe II velocity is lower, declining from 15,000 ± 550 km s^{-1} at −5 days to 4000 ± 550 km s^{-1} at +20 days.

In Figure 14 (bottom panel), the expansion velocities of SN 2020akf and SN 2021mxx measured using the Si II line are compared with other well-studied Type Ic SNe. The Si II

[15] https://github.com/tardis-sn/tardis
[16] https://github.com/tardis-sn/tardis-setups/tree/master/2022/williamson_19ewu

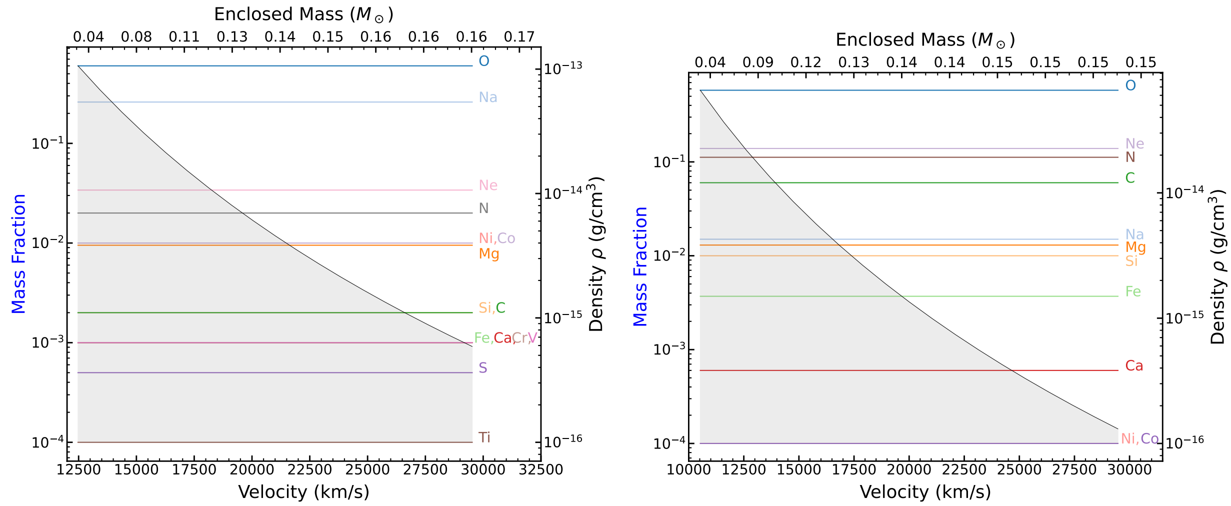

Figure 12. The TARDIS density profile (gray shaded) and the constant mass fraction of elements for SN 2020akf (left panel) at −5 days and SN 2021mxx (right panel) at −3 days are shown as a function of velocity. The top axis indicates the corresponding enclosed mass in both panels.

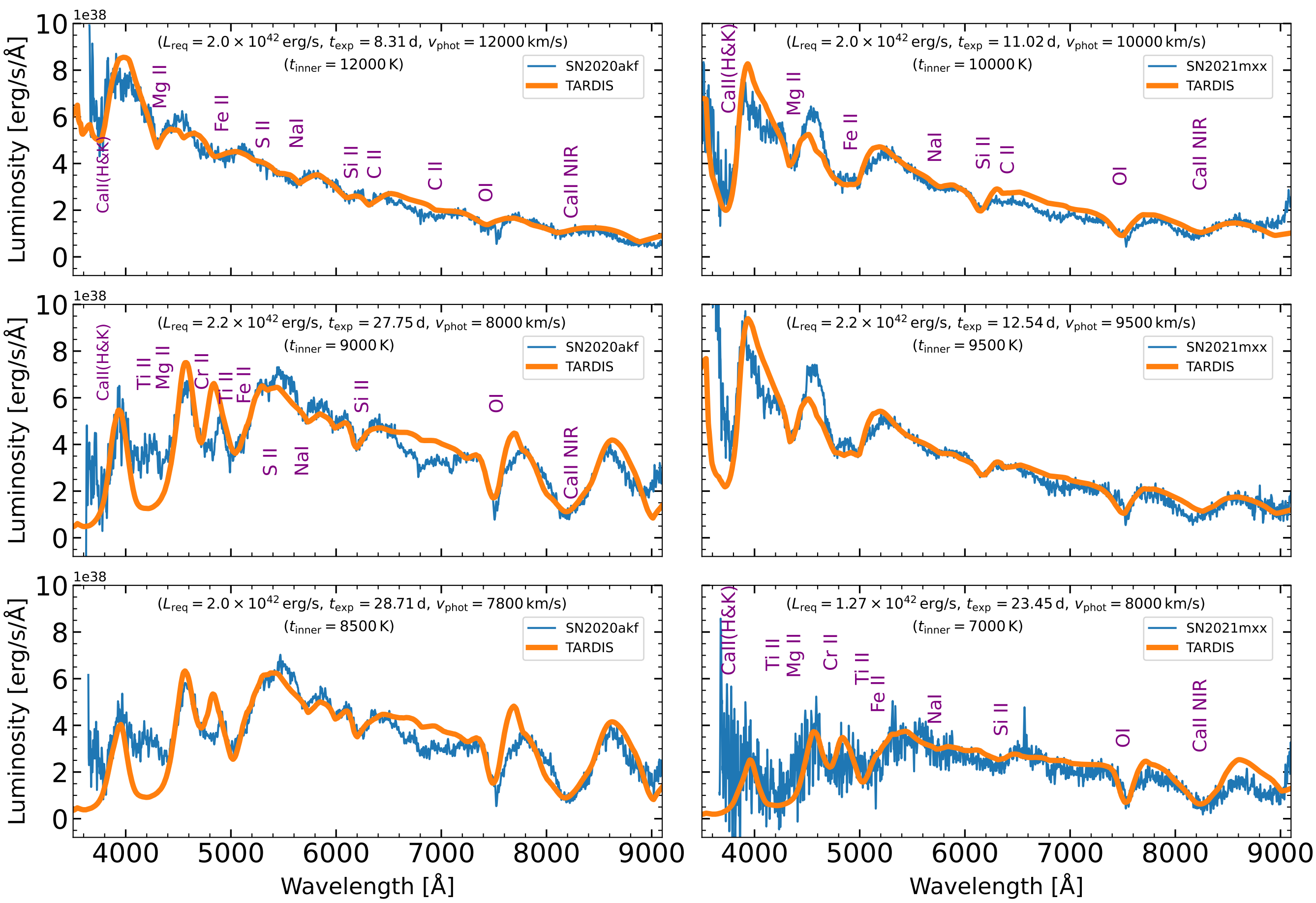

Figure 13. Observed spectral series of SN 2020akf and SN 2021mxx (blue) compared with the corresponding best-fit TARDIS synthetic spectra (orange). For each spectrum, the fitted parameters, luminosity ($L_{\rm req}$), explosion time ($t_{\rm exp}$), photospheric velocity ($v_{\rm phot}$), and inner boundary temperature ($T_{\rm inner}$) are indicated.

expansion velocities of both SN 2020akf and SN 2021mxx are within the typical range observed for normal Type Ic SNe and much lower than observed for Type Ic-BL SNe. At the peak brightness, the velocities are around $10{,}000 \pm 530$ km s^{-1} and 8500 ± 590 km s^{-1} for SN 2020akf and SN 20221mxx, respectively.

The expansion velocity of SN 2021mxx is comparable to those of SN 2007gr, SN 2014L, and SN 2017ein up to 10 days relative to *B*-maximum. SN 2020akf exhibits a higher velocity than SN 2021mxx, and its late-phase evolution closely matches that of SN 1994I.

4. Oxygen Mass

The nebular spectra of SN 2021mxx, obtained at approximately 102 and 113 days after *B*-maximum, display prominent

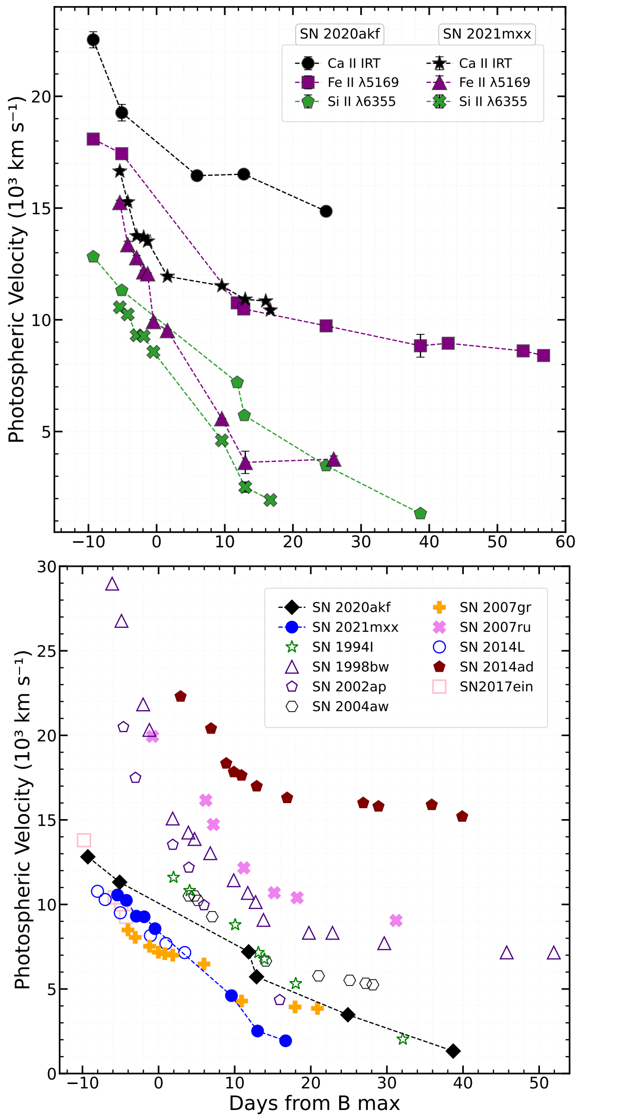

Figure 14. Top panel: evolution of the photospheric expansion velocities of SN 2020akf and SN 2021mxx, obtained from the absorption troughs of Si II, Ca II, and Fe II. Bottom panel: comparison of the photospheric velocity evolution of SN 2020akf and SN 2021mxx derived from Si II with other Type Ic SNe. The velocities of the comparison SNe are taken from their respective literature (S. Taubenberger et al. 2006; D. J. Hunter et al. 2009; D. K. Sahu et al. 2009; D. K. Sahu et al. 2018; J. Zhang et al. 2018; D. Xiang et al. 2019).

[O I] λ6300 emission lines. It is supposed to be the primary cooling agent in the late phases of Type Ib/c SNe (A. Uomoto 1986; C. Fransson & R. A. Chevalier 1987). The oxygen mass in the ejecta can be estimated from the flux of the [O I] emission line using the expression provided by A. Uomoto (1986):

$$M(\mathrm{O}) = 10^8 \times D^2 \times F([\mathrm{O\ I}]) \times \exp\left(\frac{2.28}{T_4}\right) \quad M_\odot, \qquad (2)$$

where F([O I]) represents the flux of the [O I] $\lambda\lambda$6300, 6364 lines in units of erg s^{-1} cm^{-2}, D is the distance to the SN in Mpc, and T_4 denotes the temperature of the oxygen-emitting region in units of 10^4 K. Ideally, the temperature of the oxygen-emitting region can be determined from the ratio of [O I] λ5577 to [O I] $\lambda\lambda$6300, 6364 lines.

In the nebular spectrum of SN 2021mxx, the [O I] λ5577 line is absent, constraining the line flux ratio [O I] λ5577/[O I] $\lambda\lambda$6300, 6364 to $\leqslant 0.1$. According to D. E. Osterbrock (1989), this ratio depends on the electron density and temperature of the emitting regions. The emitting region should be either at a relatively low temperature ($T_4 \leqslant 0.4$) in the high-density limit or at a low electron density ($n_e \leqslant 5 \times 10^6 \mathrm{cm}^{-3}$) with temperature $T_4 = 1$ (K. Maeda et al. 2007). In the high-density regime, using the absolute flux of [O I] $\lambda\lambda$6300, 6364 lines in the 113-day spectrum (1.53×10^{-14} erg s^{-1} cm^{-2}) and adopting a distance of 44.79 Mpc, the oxygen mass in SN 2021mxx is estimated to be 0.92 $M_\odot$.

P. A. Mazzali et al. (2010) showed that oxygen mass estimated using the flux of the [O I] $\lambda\lambda$6300, 6364 lines can be regarded as a lower limit of the total oxygen mass ejected during the explosion. Hence, 0.92 $M_\odot$ can be taken as a lower limit of the oxygen mass ejected in the explosion of SN 2021mxx.

The oxygen mass in the ejecta provides crucial insights into the progenitor's initial mass. H. Kuncarayakti et al. (2015) compared the derived oxygen masses of SNe with nucleosynthesis yields predicted for massive stars of various initial masses based on models from K. Nomoto et al. (1997), T. Rauscher et al. (2002), and M. Limongi & A. Chieffi (2003). For SN 2021mxx, the estimated oxygen mass of 0.92 $M_\odot$ suggests a progenitor mass in the range of 15–18 $M_\odot$ across all three models.

5. Metallicity of the Host Galaxy

To better understand the diverse properties of the SN region in the host galaxy, we obtained a spectrum of UGC 11380 (the host galaxy of SN 2021mxx) on 2021 September 9. For SN 2020akf, we utilized the spectrum of its host galaxy, KUG 0925+387B, obtained from the Sloan Digital Sky Survey (SDSS) Science Archive Server (SAS[17]), which was observed on 2003 December 13.

In the host galaxy spectrum of SN 2021mxx, we identified several prominent narrow emission lines, including [O III] $\lambda\lambda$4959, 5007, Hα, Hβ, [N II] λ6583, and [S II] $\lambda\lambda$6716, 6730. We used the fluxes from these narrow lines to estimate the metallicity of the host galaxy, employing well-established empirical relations from the literature, such as the N2 and O3N2 indices (M. Pettini & B. E. J. Pagel 2004). The N2 index is defined as N2 $\equiv$log([N II] λ6583/Hα), and the O3N2 index is defined as O3N2 $\equiv$log(([O III] λ5007/Hβ)/([N II] λ6583/Hα)).

For the galaxy KUG 0925+387B, the N2 index yielded an oxygen abundance of $12 + \log(\mathrm{O/H}) = 8.68$ in the host galaxy environment of SN 2020akf, while the O3N2 index gave a value of 8.59. Averaging these results, we find an oxygen abundance of $12 + \log(\mathrm{O/H}) = 8.64 \pm 0.06$, corresponding to a metallicity of 0.81 $Z_\odot$. Similarly, the oxygen abundance, $12 + \log(\mathrm{O/H})$, at the location of SN 2021mxx was estimated to be 8.60 using the N2 index and 8.59 using the O3N2 index. These values agree well with the oxygen abundance derived from the N2 index, based on host galaxy emission lines in the nebular spectrum of SN 2021mxx at ~113 days (refer to Section 3.4), which is around 8.64. The average oxygen abundance, $12 + \log(\mathrm{O/H}) = 8.61 \pm 0.03$, corresponds to a metallicity of 0.76 $Z_\odot$. This analysis suggests that the

[17] https://dr18.sdss.org/optical/spectrum/view?plateid=1214&mjd=52731&fiberid=156&run2d=26&zwarning=0&matches=any

metallicity in the host galaxy environments of SN 2020akf and SN 2021mxx is close to solar metallicity ($12 + \log(\mathrm{O/H})_\odot = 8.73$; M. Asplund et al. 2021). R. Ganss et al. (2025) have analyzed a large sample of Type Ib/Ic and Type IIP SNe to study their environments. They found mean oxygen abundances of approximately $12 + \log(\mathrm{O/H}) = 8.50$ for Type Ic SNe using both N2 and O3N2 calibrations. Thus, the host environments of SN 2020akf and SN 2021mxx fall within the observed range for Type Ic SNe.

6. Light-curve Modeling and Explosion Parameters

6.1. Arnett–Valenti Model

We estimated the synthesized ^{56}Ni mass using a modified radiation diffusion model (W. D. Arnett 1982; S. Valenti et al. 2008; E. Chatzopoulos et al. 2012). This model applies to SNe with light curves powered by radioactive decay and assumes homologous, spherical expansion of the ejecta during the photospheric phase. The model also assumes that ^{56}Ni is centrally located without mixing into the outer layers, a constant opacity, and ejecta dominated by radiation pressure. We used the modified luminosity formula from S. Valenti et al. (2008), which includes the energy contribution from ^{56}Co to ^{56}Fe decay and incorporates the gamma-ray leakage from the ejecta. The ^{56}Ni mass and effective diffusion time (τ_d), which governs the width of the bolometric light curve, were treated as free parameters.

The produced luminosity is expressed as

$$L(t) = M_{\rm Ni} e^{-x^2}\Big[(\epsilon_{\rm Ni} - \epsilon_{\rm Co}) \int_0^x 2ze^{z^2-2zy}\, dz + \epsilon_{\rm Co} \int_0^x 2ze^{z^2-2zy+2zs}\, dz\Big](1 - e^{-\left(\frac{t_\gamma}{t}\right)^2}), \quad (3)$$

where $x \equiv t_{\rm exp}/t_d$, $t_{\rm exp}$ is the time since explosion (in days) and t_d is the diffusion timescale (days). Here $y \equiv t_d/(2t_{\rm Ni})$ with $t_{\rm Ni} = 8.8$ days, and $s \equiv [t_d(t_{\rm Co} - t_{\rm Ni})]/(2t_{\rm Co}t_{\rm Ni})$ with $t_{\rm Co} = 111.3$ days. $M_{\rm Ni}$ is the Ni mass, and t_γ is the gamma-ray leakage timescale (in days). Parameters $\epsilon_{\rm Ni} = 3.9 \times 10^{10}$ erg s^{-1} g^{-1} and $\epsilon_{\rm Co} = 6.8 \times 10^9$ erg s^{-1} g^{-1} represent the energy generation rates from the radioactive decay of ^{56}Ni and ^{56}Co, respectively.

For uniform density, the kinetic energy of the ejecta (E_k) and the effective diffusion timescale (τ_d) were derived following W. D. Arnett (1982) and D. Arnett (1996), given by

$$E_k \approx \frac{3}{5}\frac{M_{\rm ej} v_{\rm ph}^2}{2} \quad (4)$$

$$\tau_d = \left(\frac{\kappa}{\beta c}\right)^{1/2}\left(\frac{6M_{\rm ej}^3}{5E_k}\right)^{1/4}, \quad (5)$$

where κ is the optical opacity, taken as 0.07 cm^2 g^{-1} (N. N. Chugai 2000); $\beta \approx 13.8$ is a constant of integration (W. D. Arnett 1982); and c is the speed of light.

To fit the quasi-bolometric light curves of SN 2020akf and SN 2021mxx, we employed a Markov Chain Monte Carlo (MCMC) approach. We utilized the `emcee` package in Python to optimize the model parameters and sample the posterior distribution, following D. Foreman-Mackey et al. (2013). The model-fitting process incorporated four key parameters: $t_{\rm exp}$ (the explosion epoch), $M_{\rm Ni}$ (the mass of ^{56}Ni synthesized), t_d (the diffusion timescale), and t_γ (the gamma-ray leakage timescale). For a detailed description of the model fit procedure, we refer to A. Dutta et al. (2022).

From the fit, we derived the following parameters for SN 2020akf: $M_{\rm Ni} = 0.12^{+0.01}_{-0.01}\,M_\odot$, $t_d = 16.83^{+0.97}_{-0.82}$ days, $t_\gamma = 43.81^{+2.04}_{-2.17}$ days, and $\mathrm{JD_{exp}} = 2{,}458{,}864.46^{+0.28}_{-0.30}$. Similarly, for SN 2021mxx, the estimated parameters are $M_{\rm Ni} = 0.05^{+0.001}_{-0.001}\,M_\odot$, $t_d = 9.03^{+0.69}_{-0.89}$ days, $t_\gamma = 42.70^{+1.31}_{-1.22}$ days, and $\mathrm{JD_{exp}} = 2{,}459{,}352.86^{+0.74}_{-0.57}$. The model fits for SN 2020akf (top panel) and SN 2021mxx (bottom panel) are shown in Figure 15, and the corresponding corner plots are shown in Figure 19 in the Appendix.

Following F. Taddia et al. (2018), Z. Cano (2013), and J. D. Lyman et al. (2016), we used the photospheric Fe II line velocities to estimate the ejecta mass ($M_{\rm ej}$) and kinetic energy (E_k) of the explosion. Taking $v_{\rm ph} = 15{,}000 \pm 700$ km s^{-1} for SN 2020akf and $10{,}000 \pm 600$ km s^{-1} for SN 2021mxx at peak brightness and applying Equations (4) and (5), we obtained $M_{\rm ej} = 4.71^{+0.50}_{-0.46}\,M_\odot$ and $E_k = 6.33^{+0.68}_{-0.62} \times 10^{51}$ erg for SN 2020akf and $M_{\rm ej} = 0.90^{+0.14}_{-0.18}\,M_\odot$ and $E_k = 0.54^{+0.08}_{-0.12} \times 10^{51}$ erg for SN 2021mxx.

6.2. MOSFiT Model

We performed multicolor light-curve modeling for SN 2020akf and SN 2021mxx using the Modular Open-Source Fitter for Transients (`MOSFiT`; J. Guillochon et al. 2018) with its `default` model, which incorporates the radioactive decay of nickel and cobalt (D. K. Nadyozhin 1994). We employed the dynamic nested sampling method, dynesty (J. S. Speagle 2020), available within `MOSFiT`, and assessed the fit quality using the likelihood score (log (Z); S. Watanabe 2010). The model contains 10 free parameters: the host galaxy hydrogen column density ($n_{\rm H,host}$), the total ejecta mass ($M_{\rm ej}$), the ^{56}Ni mass fraction ($f_{\rm Ni} \equiv M_{\rm Ni}/M_{\rm ej}$), the ejecta velocity ($v_{\rm ej}$), the γ-ray opacity (κ_γ), the explosion epoch relative to the first observation ($t_{\rm exp}$), the minimum photospheric temperature ($T_{\rm min}$), a white-noise variance term (σ), and the temporal and wavelength correlation scales (Δt and $\Delta\lambda$) that describe the Gaussian process covariance used to account for additional correlated scatter in the light-curve data. To fit the light curve, well-constrained priors were adopted, including flat, log-flat, and Gaussian. We fixed a few important parameters, such as redshift, $E(B-V)_{\rm MW}$, and luminosity–distance, for the light-curve fitting of each SN. For the better convergence,[18] `MOSFiT` was run with `-R 1.05`, ensuring convergence once the potential scale reduction factor (`PSRF`) reached 1.05. The Gelman–Rubin statistic was used to assess chain mixing, with `PSRF` values near 1 indicating well-mixed chains. This procedure improved posterior sampling by enforcing proper mixing. The sampling utilized 2000 walkers until convergence was achieved. A detailed description of the model-fitting procedure is provided in J. Guillochon et al. (2018) and recent studies, such as S. Srivastav et al. (2023), K. W. Davis et al. (2023), A. Gkini et al. (2024), and T. Moore et al. (2025).

The multicolor light curves of SN 2020akf (top panel) and SN 2021mxx (bottom panel) with fitted models are displayed in Figure 16. The associated corner plots are shown in Figures 20 and 21, respectively, in the Appendix. The optimized model reproduced the observed light curves of both SNe reasonably well in the early phase ∼30 days after

[18] https://mosfit.readthedocs.io/en/latest/assessing.html

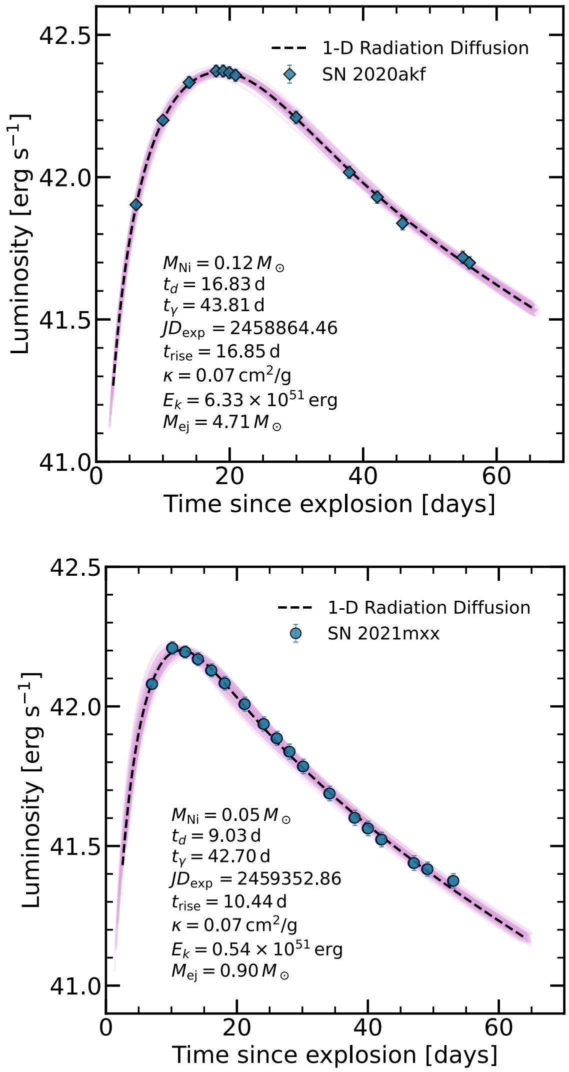

Figure 15. The quasi-bolometric light curves of SN 2020akf (top panel) and SN 2021mxx (bottom panel) are fitted using the Arnett–Valenti model. The estimated parameters are presented below the fit.

maximum, except c and o bands in SN 2020akf and o band in SN 2021mxx. However, in the later phases, some deviation is seen, especially in the redder bands, such as o and I bands. From the MOSFiT model, for SN 2020akf, the synthesized ^{56}Ni mass ($M_{\rm Ni} = f_{\rm Ni} \times M_{\rm ej}$) and the ejecta masses ($M_{\rm ej}$) are estimated to be $0.20^{+0.07}_{-0.05}\,M_\odot$ and $3.16^{+0.55}_{-0.47}\,M_\odot$, respectively. For SN 2021mxx, the corresponding quantities are $0.09^{+0.02}_{-0.01}$ $M_\odot$ and $1.53^{+0.18}_{-0.17}\,M_\odot$. The other estimated parameters and priors for both SNe are summarized in Table 7 in the Appendix. There is a slight difference between the $M_{\rm Ni}$ and $M_{\rm ej}$ values estimated using MOSFiT and those from the W. D. Arnett (1982) model, which may be due to variations in $t_{\rm exp}$ and $v_{\rm ej}$ in the two models. However, they are consistent within 3σ uncertainties.

7. Discussion and Summary

We present a comprehensive optical photometric and spectroscopic analysis of two Type Ic SNe, 2020akf and 2021mxx.

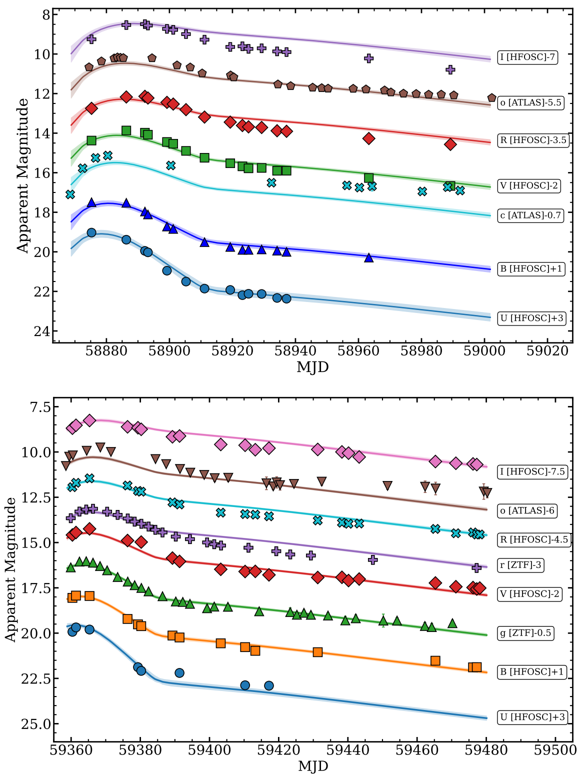

Figure 16. The multiband *U BcV RoI* light curves of SN 2020akf (top panel) and *U BgV r RoI* light curves of SN 2021mxx (bottom panel) are fitted with the default MOSFiT model. The plotted lines show the median MOSFiT light-curve fits, and the shaded regions indicate the 5%–95% confidence intervals for each band during the first 120 days.

7.1. SN 2020akf

SN 2020akf exhibits broader light curves across the $UBVRI$ bands, indicating a slower decline in brightness. The absolute V-band magnitude of SN 2020akf ($M_V = -17.85 \pm 0.15$ mag) and its quasi-bolometric luminosity ($\log L_{\rm bol}^{\rm max} = 42.37 \pm 0.02$ erg s^{-1}) are on the higher side compared to many well-sampled Type Ic SNe but lower than those of Type Ic-BL SNe. This places SN 2020akf in the category of transitional Type Ic SNe, between the normal Type Ic and Type Ic-BL SNe, similar to SN 2004aw (S. Taubenberger et al. 2006). The spectral evolution of SN 2020akf exhibits prominent Si II and C II lines, which we could reproduce using TARDIS. Similar spectral features have been observed in the early spectra of SN 2007gr (J. Chen et al. 2014) and SN 2004aw (S. Taubenberger et al. 2006).

Previous investigations by M. Williamson et al. (2023) noted spectroscopic similarities between SN 2020akf and two SE superluminous SNe (SLSNe Ic), iPTF 13ajg (P. M. Vreeswijk et al. 2014) and SSS 120810–23 (M. Nicholl et al. 2014), and also discussed the presence of O II features in the early spectra of SN 2020akf, which are generally found in SLSNe Ic. Using TARDIS, we examined the presence of O II lines and found that the observed features are more consistent with Mg II lines. Comparisons of photometric and spectroscopic properties of SN 2020akf with those of well-studied SLSNe Ic (e.g., L. Yan et al. 2015; P. A. Mazzali et al. 2016; Y.-Q. Liu et al. 2017) suggest that it does not exhibit the features of superluminous events, while it shares the majority of characteristics of Type Ic SNe (e.g., S. J. Prentice et al. 2016).

To understand the progenitor properties, we estimated the explosion parameters using the Ni decay model of W. D. Arnett (1982) and D. Arnett (1996) and the MOSFiT tool. With the updated Arnet–Valenti model, the amount of radioactive ^{56}Ni synthesized is $M_{\rm Ni} = 0.12^{+0.01}_{-0.01}\,M_\odot$, the ejected mass during the explosion is $M_{\rm ej} = 4.71^{+0.50}_{-0.46}\,M_\odot$, and the kinetic energy is $E_k = 6.33^{+0.68}_{-0.62} \times 10^{51}$ erg. The diffusion timescale is estimated to be $t_d = 16.83^{+0.97}_{-0.82}$ days. The higher diffusion time for SN 2020akf indicates a denser, higher-opacity environment consistent with its larger ejected mass. Using the *default* model in MOSFiT, we estimated $M_{\rm Ni} = 0.20^{+0.07}_{-0.05}\,M_\odot$ and $M_{\rm ej} = 3.16^{+0.55}_{-0.47}\,M_\odot$. From both modeling approaches, we find that the inferred explosion parameters are consistent within the 3σ uncertainties. The metallicity estimates based on the N2 and O3N2 indices suggest that SN 2020akf exploded in a region with nearly solar metallicity. Due to the nonavailability of late-phase data of SN 2020akf, it is difficult to estimate the mass of its progenitor star. However, taking into account the estimated mass of the ejecta of $\sim$4 $M_\odot$ and assuming that the mass of the neutron star formed after explosion is $\sim$2 $M_\odot$, the mass of the core at the time of explosion would be $\sim$6 $M_\odot$.

7.2. SN 2021mxx

SN 2021mxx exhibits narrower light curves with a rapid rise and a faster decline, similar to those of Type Ic SNe SN 1994I, SN 2014L, and SN 2007gr. It attained peak *V*-band absolute magnitude ($M_V = -17.60 \pm 0.15$ mag) and quasi-bolometric luminosity ($\log L_{\rm bol}^{\rm max} = 42.21 \pm 0.02\,{\rm erg\,s^{-1}}$). The Arnet–Valenti model fit gives $M_{\rm Ni} = 0.05^{+0.00}_{-0.00}\,M_\odot$, $M_{\rm ej} = 0.90^{+0.14}_{-0.18}\,M_\odot$, and $E_k = 0.54^{+0.08}_{-0.12} \times 10^{51}$ erg. The estimated diffusion time $t_d = 9.03^{+0.69}_{-0.89}$ days suggests that SN 2021mxx exhibits a rapid rise. The *default* model in MOSFiT gives $M_{\rm Ni} = 0.09^{+0.02}_{-0.02}\,M_\odot$ and $M_{\rm ej} = 1.53^{+0.18}_{-0.17}\,M_\odot$, indicating that the inferred explosion parameters are consistent within the uncertainties 3σ in both models.

The prominent features identified in the spectra of SN 2021mxx are identical to those of Type Ic events SN 1994I, SN 2004aw, and SN 2017ein and were successfully reproduced using TARDIS. The estimated ejecta velocity at peak brightness and its evolution are comparable to those of SN 2007gr and SN 2014L.

Analysis of the nebular-phase spectrum of SN 2021mxx, observed 123 days post-explosion, reveals an [O I]/[Ca II] line ratio of approximately 0.96, indicating a lower-mass progenitor for this SN. Using the absolute flux of the [O I] λ6300 line, the estimated mass of oxygen in the ejecta is $\sim$0.92 $M_\odot$, which indicates a ZAMS mass of the progenitor star in the range of 15–18 $M_\odot$. We compared the nebular-phase spectrum of SN 2021mxx with the nebular-phase model spectra from A. Jerkstrand et al. (2015). The best-fitting model indicates that the progenitor mass is in the range of 13–17 $M_\odot$. Hence, the mass range of the progenitor star could be taken as 13–18 $M_\odot$. The metallicity of the host galaxy in the SN region is found to be nearly solar.

In Figure 17, the distributions of $M_{\rm ej}$–E_k for well-studied Type Ibc, Type Ic-BL, and GRB/X-ray Flash (XRF) SNe, taken from Z. Cano (2013), J. D. Lyman et al. (2016), F. Taddia et al. (2018, 2019), and E. Karamehmetoglu et al. (2023), has been plotted along with those of SN 2020akf and SN 2021mxx. Z. Cano (2013) found that Type Ibc SNe

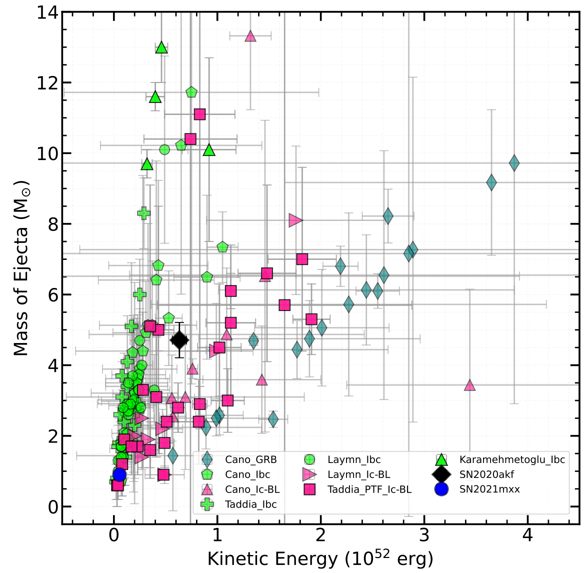

Figure 17. The ejecta mass ($M_{\rm ej}$) and kinetic energy (E_k) for SN 2020akf and SN 2021mxx are plotted along with those of other well-studied Type Ic, Type Ic-BL, and GRB/XRF SNe. The sample data are taken from Z. Cano (2013), J. D. Lyman et al. (2016), F. Taddia et al. (2018, 2019), and E. Karamehmetoglu et al. (2023).

typically exhibit a median ejecta mass of $M_{\rm ej} \sim 3.4$–$3.9\,M_\odot$, a kinetic energy of $E_k \sim 0.2 \times 10^{52}$ erg, and a characteristic $E_k/M_{\rm ej}$ ratio of $\sim$0.06 in units of ($10^{52}\,{\rm erg}/M_\odot$). For SN 2020akf, we derive $E_k/M_{\rm ej} \sim 0.134$, which is comparable to that of SN 2004aw (0.134). However, with $E_k/M_{\rm ej} \sim 0.06$, SN 2021mxx shows a value more consistent with the well-studied, typical Type Ic SNe, such as SN 2005mf (0.063), SN 2007gr (0.064), and SN 2011bm (0.063). The explosion parameters of both SNe are broadly consistent with those of Type Ib/c SNe and fall well within the region occupied by this class. However, SN 2021mxx lies distinctly in the parameter space, characterized by very low $M_{\rm ej}$ and E_k.

Acknowledgments

We thank the referee for carefully reading the manuscript and providing constructive suggestions that helped in improving the manuscript. We express our gratitude to the Director and Dean of IIA, Bengaluru, for their generous hospitality and the facilities provided. We appreciate the assistance of IIA staff at CREST and IAO during our observations, as well as the observers of the 2 m HCT who kindly allocated part of their observing time for SN studies. D.K.S. acknowledges financial support from the CRG/ 2022/007688 project grant. N.K.C. acknowledges IUCAA, Pune, for providing facilities through its Visiting Associate Program. M.S. acknowledges financial support provided under the National Post Doctoral Fellowship (N-PDF; File Number: PDF/2023/002244) by the Science & Engineering Research Board (SERB), Anusandhan National Research Foundation (ANRF), Government of India. This work has utilized data from the NASA Astrophysics Data System (ADS), the NASA/IPAC Infrared Science Archive (IRSA), and the NASA/IPAC Extragalactic Database (NED), which are operated by the Jet Propulsion Laboratory, California Institute of Technology, under contract with the National Aeronautics and Space Administration. We have utilized the Weizmann Interactive Supernova Data Repository (WISeREP) and data from ZTF, ATLAS, and SDSS.

Data Availability

The data presented in this article will be shared on request to the corresponding author. All spectra will be made publicly available through WISeREP.

Facilities: 2meter Himalayan Chandra Telescope (HCT) at the Indian Astronomical Observatory (IAO), Hanle, India.

Software: IRAF (D. Tody 1993), TARDIS (W. E. Kerzendorf & S. A. Sim 2014; C. Vogl et al. 2019), MOSFiT (J. Guillochon et al. 2018), SuperBol (M. Nicholl 2018), Matplotlib (J. D. Hunter 2007), Numpy (S. van der Walt et al. 2011), Astropy (Astropy Collaboration et al. 2013, 2018; Astropy Collaboration et al. 2022), Scipy (P. Virtanen et al. 2020), scikit-learn (F. Pedregosa et al. 2011), corner (D. Foreman-Mackey 2016), emcee (D. Foreman-Mackey et al. 2013).

Appendix

This section includes tables 1–7 containing key observational and derived properties of SN 2020akf, SN 2021mxx, and their host galaxies; apparent magnitudes of secondary standard stars; photometric measurements and derived parameters of the SNe; logs of spectroscopic observations; and the model parameters and priors adopted in the MOSFiT analysis. It also includes figures 18–21 showing the convergence profiles of the TARDIS models and the corner plots for the Arnett–Valenti and MOSFiT model fits.

Table 1
Important Parameters of SN 2020akf, SN 2021mxx, and their Host Galaxies

	SN 2020akf		SN 2021mxx	
Parameters	Values	References	Values	References
Discovery date	2020-01-20 12:04:19 (JD 2,458,869.0)	(1)	2021-05-22 09:22:03 (JD 2,459,356.9)	(6)
R.A. (J2000)	09:28:39.6	(1)	18:56:51.3	(6)
Decl. (J2000)	38:33:47.1	(1)	36:37:20.4	(6)
Explosion date	JD $2,458,864.46^{+0.28}_{-0.30}$	(2)	JD $2,459,352.86^{+0.74}_{-0.57}$	(2)
Date of *B*-maximum	JD 2,458,880.4 ± 0.5	(2)	JD 2,459,363.3 ± 0.5	(2)
$\Delta m_{15}(B)$	0.98 ± 0.02	(2)	1.52 ± 0.03	(2)
Galactic reddening	0.013 ± 0.001 mag	(3)	0.08 ± 0.002 mag	(3)
Host reddening	Negligible	(2)	0.12 ± 0.03 mag	(2)
$E(B-V)_{\rm total}$	0.013 ± 0.001 mag	(2)	0.20 ± 0.03 mag	(2)
$m_B^{\rm max}$	16.34 ± 0.02 mag	(2)	16.90 ± 0.03 mag	(2)
$M_V^{\rm max}$	−17.85 ± 0.15 mag	(2)	−17.60 ± 0.15 mag	(2)
$\log L_{\rm quasi\text{-}bol}^{\rm max}$	42.37 ± 0.02 erg s^{-1}	(2)	42.21 ± 0.02 erg s^{-1}	(2)
^{56}Ni mass	0.10 ± 0.02 $M_\odot$	(2)	0.05 ± 0.01 $M_\odot$	(2)
Ejected mass ($M_{\rm ej}$)	$4.71^{+0.50}_{-0.46}$ $M_\odot$	(2)	$0.90^{+0.14}_{-0.18}$ $M_\odot$	(2)
$v_{\rm max}$(Fe II λ5169)	15,000 km s^{-1}	(2)	10,000 km s^{-1}	(2)
Kinetic energy (E_k)	$6.33^{+0.68}_{-0.62} \times 10^{51}$ erg	(2)	$0.54^{+0.08}_{-0.12} \times 10^{51}$ erg	(2)
	KUG 0925+387B		UGC 11380	
Type	Spiral-Sc	(4)	Spiral-Sab	(4)
R.A. (J2000)	09:28:39.8	(5)	18:56:51.1	(5)
Decl. (J2000)	38:33:49.0	(5)	36:37:26.3	(5)
$z_{\rm helio}$	0.012445 ± 0.000011	(5)	0.009650 ± 0.000060	(5)
$v_{\rm Virgo}$	3903 ± 14 km s^{-1}	(5)	3,225 ± 25 km s^{-1}	(5)
Distance	54.21 ± 4 Mpc	(5)[a]	44.79 μ 3 Mpc	(5)[a]
Distance modulus	33.67 ± 0.15 mag	(5)[a]	33.26 ± 0.15 mag	(5)[a]

References. (1) J. Tonry et al. (2020); (2) this work; (3) E. F. Schlafly & D. P. Finkbeiner (2011); (4) Hyperleda; (5) NED 5[a], using $H_0 = 72$ km s^{-1} Mpc^{-1}; (6) F. Forster et al. (2021).

Table 2
Magnitudes of Secondary Standard Stars in the Fields of SN 2020akf and SN 2021mxx

ID	R.A.	Decl.	*U*	*B*	*V*	*R*	*I*
			SN 2020akf				
1	09 28 30.7	+38 33 22.7	14.43 ± 0.04	14.56 ± 0.07	14.09 ± 0.06	13.77 ± 0.08	13.46 ± 0.09
2	09 28 36.6	+38 29 41.8	15.35 ± 0.05	15.40 ± 0.07	14.82 ± 0.07	14.44 ± 0.09	14.08 ± 0.12
3	09 28 27.9	+38 29 50.4	16.48 ± 0.06	15.85 ± 0.09	14.94 ± 0.08	14.42 ± 0.11	13.94 ± 0.14
4	09 28 42.5	+38 32 23.3	16.65 ± 0.04	15.92 ± 0.08	15.01 ± 0.07	14.51 ± 0.10	14.07 ± 0.12
5	09 28 38.2	+38 31 44.0	16.64 ± 0.05	15.98 ± 0.08	15.10 ± 0.08	14.58 ± 0.08	14.10 ± 0.10
6	09 28 22.1	+38 32 45.1	16.42 ± 0.05	16.08 ± 0.08	15.24 ± 0.07	14.75 ± 0.11	14.28 ± 0.13
			SN 2021mxx				
1	18 56 38.1	+36 38 17.3	15.56 ± 0.02	15.16 ± 0.02	14.37 ± 0.02	13.90 ± 0.02	13.46 ± 0.02
2	18 56 44.2	+36 40 23.7	15.19 ± 0.02	15.01 ± 0.02	14.36 ± 0.01	13.96 ± 0.02	13.61 ± 0.01
3	18 56 44.6	+36 40 41.7	15.72 ± 0.02	15.54 ± 0.02	14.86 ± 0.01	14.46 ± 0.03	14.07 ± 0.03
4	18 56 52.6	+36 35 57.2	16.08 ± 0.02	15.76 ± 0.02	15.02 ± 0.01	14.59 ± 0.01	14.20 ± 0.02
5	18 56 43.8	+36 35 37.0	15.27 ± 0.01	15.39 ± 0.02	14.84 ± 0.01	14.46 ± 0.01	14.08 ± 0.02
6	18 56 38.8	+36 37 01.2	16.32 ± 0.03	15.89 ± 0.01	15.12 ± 0.01	14.67 ± 0.02	14.26 ± 0.02
7	18 56 50.6	+36 36 16.1	16.92 ± 0.02	16.44 ± 0.02	15.53 ± 0.02	15.02 ± 0.02	14.52 ± 0.02
8	18 56 56.2	+36 40 03.1	16.01 ± 0.03	15.93 ± 0.01	15.30 ± 0.01	14.92 ± 0.01	14.54 ± 0.01
9	18 56 30.8	+36 39 11.4	19.80 ± 0.10	18.57 ± 0.01	17.05 ± 0.02	16.01 ± 0.01	14.85 ± 0.01
10	18 56 52.4	+36 38 25.6	16.75 ± 0.02	16.23 ± 0.03	15.42 ± 0.01	14.93 ± 0.01	14.48 ± 0.02

Note. The stars are marked in Figure 1.

Table 3
Optical *U BV RI* Photometric Observations of SN 2020akf with HCT

Date	JD[a]	Phase[b]	*U*	*B*	*V*	*R*	*I*
26/01/2020	8875.28	−5.1	16.03 ± 0.01	16.49 ± 0.01	16.38 ± 0.02	16.25 ± 0.01	16.26 ± 0.04
06/02/2020	8886.32	5.9	16.39 ± 0.12	16.52 ± 0.02	15.87 ± 0.02	15.67 ± 0.02	15.54 ± 0.03
12/02/2020	8892.22	11.8	16.95 ± 0.04	16.96 ± 0.02	15.98 ± 0.02	15.64 ± 0.02	15.49 ± 0.02
13/02/2020	8893.18	12.8	17.03 ± 0.02	17.11 ± 0.02	16.08 ± 0.02	15.72 ± 0.02	15.56 ± 0.03
19/02/2020	8899.22	18.9	17.96 ± 0.03	17.72 ± 0.01	16.45 ± 0.01	15.94 ± 0.02	15.73 ± 0.02
21/02/2020	8901.20	20.9	⋯	17.84 ± 0.02	16.54 ± 0.03	16.03 ± 0.03	15.78 ± 0.03
25/02/2020	8905.26	24.9	18.50 ± 0.04	⋯	16.90 ± 0.02	16.31 ± 0.03	15.99 ± 0.03
02/03/2020	8911.14	30.8	18.86 ± 0.05	18.51 ± 0.02	17.24 ± 0.02	16.69 ± 0.03	16.28 ± 0.03
10/03/2020	8919.30	39.0	18.93 ± 0.08	18.75 ± 0.04	17.52 ± 0.02	16.94 ± 0.02	16.64 ± 0.04
14/03/2020	8923.17	42.8	19.19 ± 0.05	18.90 ± 0.02	17.68 ± 0.02	17.11 ± 0.02	16.61 ± 0.03
16/03/2020	8925.10	44.8	19.12 ± 0.05	18.90 ± 0.03	17.78 ± 0.03	17.18 ± 0.02	16.74 ± 0.02
20/03/2020	8929.27	48.9	19.13 ± 0.13	18.88 ± 0.02	17.76 ± 0.02	17.21 ± 0.03	16.71 ± 0.03
25/03/2020	8934.17	53.8	19.33 ± 0.06	18.94 ± 0.15	17.90 ± 0.02	17.38 ± 0.03	16.87 ± 0.02
28/03/2020	8937.17	56.8	19.37 ± 0.06	19.00 ± 0.02	17.90 ± 0.03	17.41 ± 0.03	16.90 ± 0.03
23/04/2020	8963.30	83.0	⋯	19.29 ± 0.03	18.27 ± 0.02	17.77 ± 0.02	17.22 ± 0.03
19/05/2020	8989.19	108.8	⋯	⋯	18.67 ± 0.02	18.07 ± 0.02	17.79 ± 0.02

Notes.
[a] JD −2,450,000.
[b] Observed phase with respect to the epoch of *B*-band maximum: JD = 2,458,880.4.

Table 4
Optical *U BV RI* Photometric Observations of SN 2021mxx with HCT

Date	JD[a]	Phase[b]	U	B	V	R	I
25/05/2021	9360.38	−2.9	16.93 ± 0.12	17.05 ± 0.02	16.58 ± 0.01	16.44 ± 0.02	16.19 ± 0.02
26/05/2021	9361.41	−1.9	16.68 ± 0.03	16.93 ± 0.03	16.45 ± 0.02	16.20 ± 0.02	16.03 ± 0.11
30/05/2021	9365.33	2.0	16.80 ± 0.06	16.95 ± 0.03	16.24 ± 0.02	15.95 ± 0.01	15.76 ± 0.03
10/06/2021	9376.31	13.0	⋯	18.22 ± 0.01	16.89 ± 0.02	16.35 ± 0.02	16.11 ± 0.02
13/06/2021	9379.32	16.0	18.88 ± 0.13	18.52 ± 0.03	⋯	16.65 ± 0.02	16.16 ± 0.02
14/06/2021	9380.26	16.9	19.08 ± 0.16	18.61 ± 0.02	16.97 ± 0.02	16.69 ± 0.01	16.25 ± 0.02
23/06/2021	9389.30	25.9	⋯	19.13 ± 0.06	17.86 ± 0.03	17.28 ± 0.02	16.66 ± 0.08
25/06/2021	9391.34	28.0	19.20 ± 0.17	19.24 ± 0.09	18.04 ± 0.02	17.40 ± 0.02	16.62 ± 0.10
07/07/2021	9403.25	39.9	⋯	19.56 ± 0.07	18.48 ± 0.02	17.85 ± 0.02	17.09 ± 0.02
14/07/2021	9410.29	46.7	19.88 ± 0.17	19.77 ± 0.04	18.60 ± 0.03	17.93 ± 0.03	17.13 ± 0.12
17/07/2021	9413.24	49.9	⋯	19.98 ± 0.07	18.59 ± 0.03	17.96 ± 0.03	17.38 ± 0.05
21/07/2021	9417.19	53.9	19.90 ± 0.20	⋯	18.78 ± 0.04	18.05 ± 0.03	17.29 ± 0.09
04/08/2021	9431.29	67.9	⋯	20.05 ± 0.03	18.93 ± 0.02	18.28 ± 0.03	17.36 ± 0.10
11/08/2021	9438.28	74.9	⋯	⋯	18.92 ± 0.03	18.41 ± 0.03	17.50 ± 0.12
13/08/2021	9440.19	76.9	⋯	⋯	19.10 ± 0.02	18.46 ± 0.03	17.56 ± 0.14
16/08/2021	9443.27	79.9	⋯	⋯	19.01 ± 0.02	18.45 ± 0.03	17.78 ± 0.03
07/09/2021	9465.30	101.9	⋯	20.52 ± 0.06	19.23 ± 0.05	18.75 ± 0.14	18.03 ± 0.20
13/09/2021	9471.21	107.9	⋯	⋯	19.44 ± 0.04	18.99 ± 0.04	18.12 ± 0.09
18/09/2021	9476.17	112.9	⋯	20.89 ± 0.09	19.48 ± 0.04	18.94 ± 0.14	18.16 ± 0.11
19/09/2021	9477.25	113.9	⋯	20.88 ± 0.13	19.56 ± 0.05	19.06 ± 0.07	18.20 ± 0.12
20/09/2021	9478.12	114.8	⋯	⋯	19.51 ± 0.05	19.05 ± 0.05	18.61 ± 0.07

Notes.
[a] JD −2,450,000.
[b] Observed phase with respect to the epoch of *B*-band maximum: JD = 2,459,363.3.

Table 5
Photometric Parameters of SN 2020akf and SN 2021mxx

Band	JD (max)[a]	$m_\lambda^{\max}$	$M_\lambda^{\max}$	$\Delta m_{15}(\lambda)$
		SN 2020akf		
U	8878.6 ± 0.5	15.95 ± 0.09	−17.72 ± 0.16	1.20 ± 0.08
B	8880.4 ± 0.5	16.34 ± 0.02	−17.38 ± 0.15	0.98 ± 0.02
V	8886.2 ± 0.5	15.86 ± 0.02	−17.85 ± 0.15	0.69 ± 0.03
R	8889.0 ± 0.5	15.64 ± 0.02	−18.06 ± 0.15	0.58 ± 0.03
I	8889.7 ± 0.5	15.48 ± 0.03	−18.21 ± 0.15	0.48 ± 0.04
		SN 2021mxx		
U	9362.8 ± 0.5	16.64 ± 0.06	−17.58 ± 0.16	1.96 ± 0.10
B	9363.3 ± 0.5	16.90 ± 0.03	−17.14 ± 0.17	1.52 ± 0.03
V	9365.1 ± 0.5	16.25 ± 0.02	−17.60 ± 0.15	0.74 ± 0.03
R	9366.8 ± 0.5	15.93 ± 0.02	−17.84 ± 0.15	0.89 ± 0.02
I	9366.8 ± 0.5	15.74 ± 0.04	−17.87 ± 0.16	0.54 ± 0.05

Note.
[a] JD −2,450,000.

Table 6
Log of Spectroscopic Observations of SN 2020akf and SN 2021mxx with HCT

Date	JD[a]	Phase[b]	Range (Å)
		SN 2020akf	
26/01/2020	8875.27	−5.1	3500–7800; 5200–9250
12/02/2020	8892.21	11.8	3500–7800; 5200–9250
13/02/2020	8893.17	12.8	3500–7800; 5200–9250
19/02/2020	8899.21	18.8	3500–7800
25/02/2020	8905.26	24.9	3500–7800; 5200–9250
09/03/2020	8918.22	37.8	3500–7800; 5200–9250
14/03/2020	8923.16	42.8	3500–7800; 5200–9250
25/03/2020	8934.16	53.8	3500–7800; 5200–9250
28/03/2020	8937.16	56.8	3500–7800; 5200–9250
		SN 2021mxx	
25/05/2021	9360.38	−2.9	3500–7800; 5200–9250
26/05/2021	9361.40	−1.9	3500–7800; 5200–9250
10/06/2021	9376.31	13.0	3500–7800; 5200–9250
13/06/2021	9379.31	17.0	3500–7800; 5200–9250
23/06/2021	9389.29	26.0	3500–7800; 5200–9250
25/06/2021	9391.34	28.0	3500–7800
07/07/2021	9403.25	39.9	3500–7800; 5200–9250
14/07/2021	9410.29	47.0	3500–7800
16/07/2021	9412.29	49.9	3500–7800; 5200–9250
28/08/2021	9455.12	91.8	5200–9250
07/09/2021	9465.29	102.0	5200–9250
18/09/2021	9476.17	112.9	5200–9250

Notes.
[a] JD −2,450,000.
[b] Phase in days relative to *B*-maximum.

Table 7
Various Parameters and Priors Used in the MOSFiT *Default* Model for SN 2020akf and SN 2021mxx

Parameter	Prior Type and Priors	Results
	SN 2020akf	
f_{Ni}	log-flat $[10^{-3}, 1]$	$0.06^{+0.01}_{-0.01}$
M_{ej}	log-flat $[10^{-2}, 100]$	$3.16^{+0.55}_{-0.47}$
κ_{γ}	G $[\mu = 0.06, \sigma{=}0.01, (10^{-3}, 10^{4})]$	$0.06^{+0.001}_{-0.001}$
v_{ej}	G $[\mu = 10^{4}, \sigma{=}2000, (2 \times 10^{3}, 15 \times 10^{5})]$	7519.88^{+687}_{-644}
T_{min}	flat $[3.5 \times 10^{2}, 10^{5}]$	$4074.03^{+92.54}_{-86.25}$
σ	log-flat $[10^{-2}, 1]$	$0.36^{+0.03}_{-0.02}$
t_{exp} (days)	flat $[-15, 10]$	$-7.59^{+1.23}_{-1.44}$
Score log(Z)	…	36.24
	SN 2021mxx	
f_{Ni}	log-flat $[10^{-2}, 0.15]$	$0.06^{+0.01}_{-0.01}$
M_{ej}	flat $[10^{-2}, 10]$	$1.53^{+0.18}_{-0.17}$
κ_{γ}	G $[\mu = 0.06, \sigma = 0.01, (10^{-2}, 10^{4}]$	$0.06^{+0.001}_{-0.001}$
V_{ej}	G $[\mu = 10^{4}, \sigma = 2000, (2{\times}10^{3}, 15{\times}10^{5})]$	7958.62^{+584}_{-531}
T_{min}	log-flat $[3.5 \times 10^{3}, 10^{6}]$	3981^{+93}_{-91}
σ	log-flat $[10^{-2}, 1]$	$0.25^{+0.02}_{-0.02}$
t_{exp} (days)	flat $[-15, 10]$	$-10.14^{+0.71}_{-0.78}$
Score log(Z)	…	113

Note. "G" denotes a Gaussian distribution, and most of the priors are in log space; see corner plots in Figures 20 and 21 for reference.

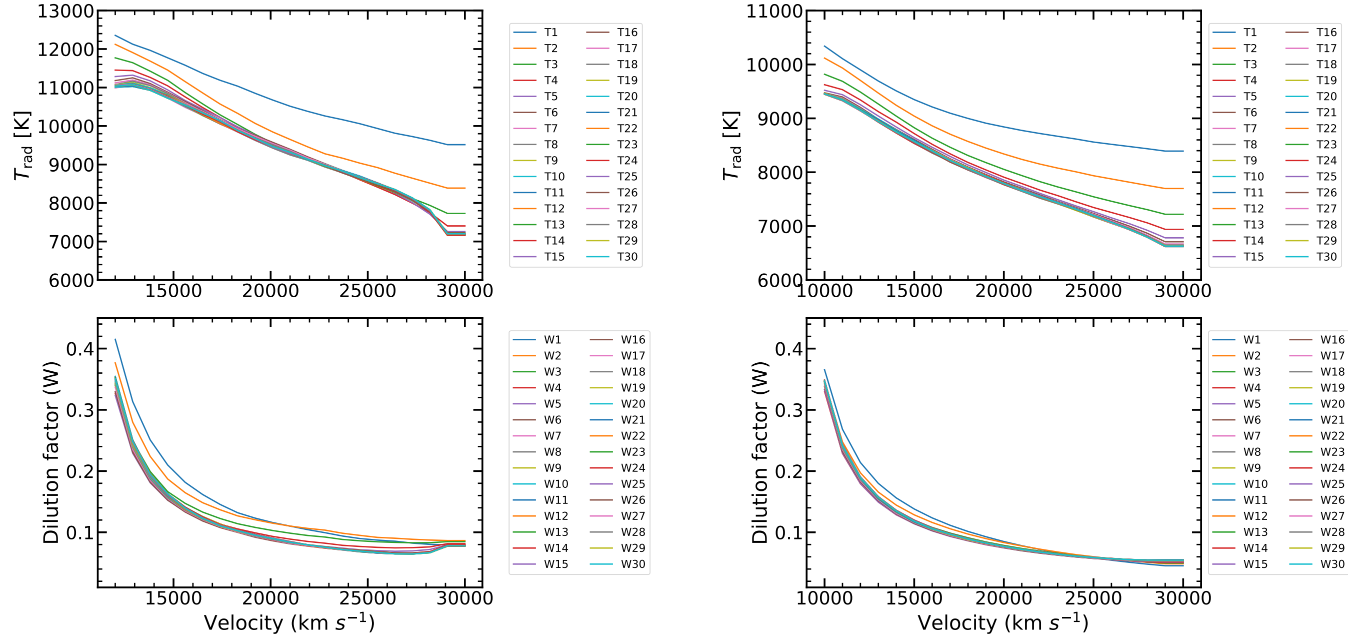

Figure 18. Convergence profiles of the TARDIS model for SN 2020akf at −5 days (left column) and SN 2021mxx at −3 days (right column). The top panels show the distribution of the radiation temperature ($T_{\rm rad}$), and the bottom panels present the corresponding dilution factor (W) as a function of velocity.

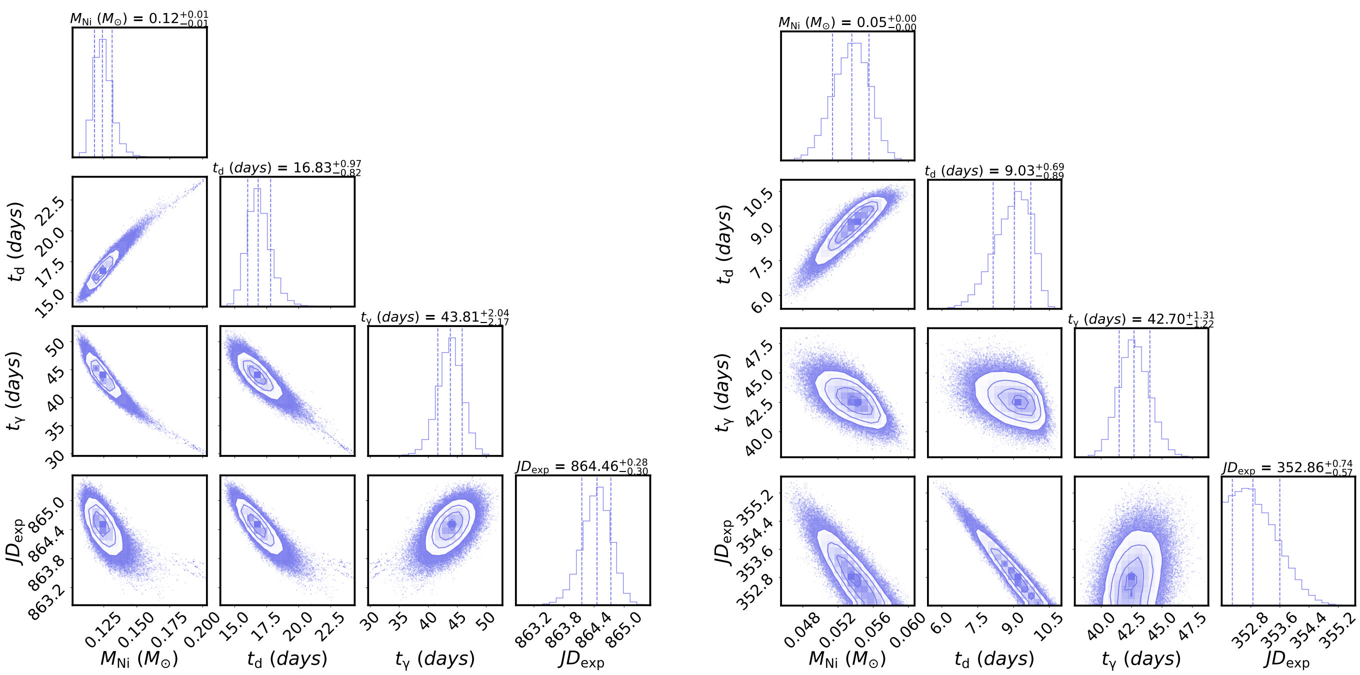

Figure 19. The 1D and 2D posterior distributions of the parameters in the Arnett–Valenti model fit. The median values and 1σ confidence intervals are marked, highlighting the best-fit values of key physical parameters, including the nickel mass ($M_{\rm Ni}$), diffusion time (t_d), gamma-ray leakage timescale (t_γ), and explosion epoch ($\rm JD_{exp}$) for SN 2020akf (left column) and SN 2021mxx (right column).

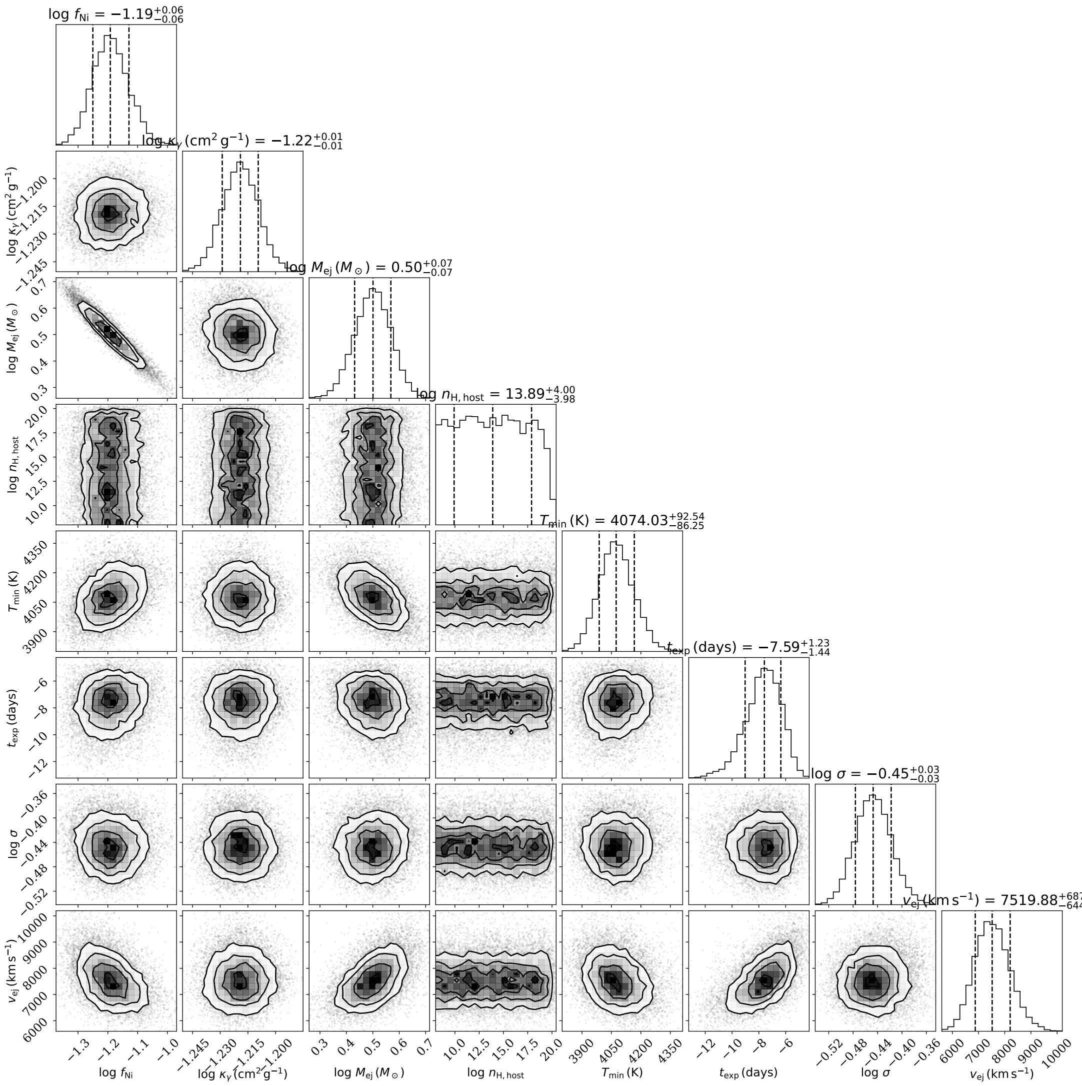

Figure 20. The 1D and 2D posterior distributions of the *default* ^{56}Ni model parameters in MOSFiT used for SN 2020akf. The median and 1σ confidence intervals are marked to indicate the best-fit values of important physical parameters such as nickel fraction f_{Ni}, ejecta mass M_{ej}, k, k_γ, t_{exp}, etc.

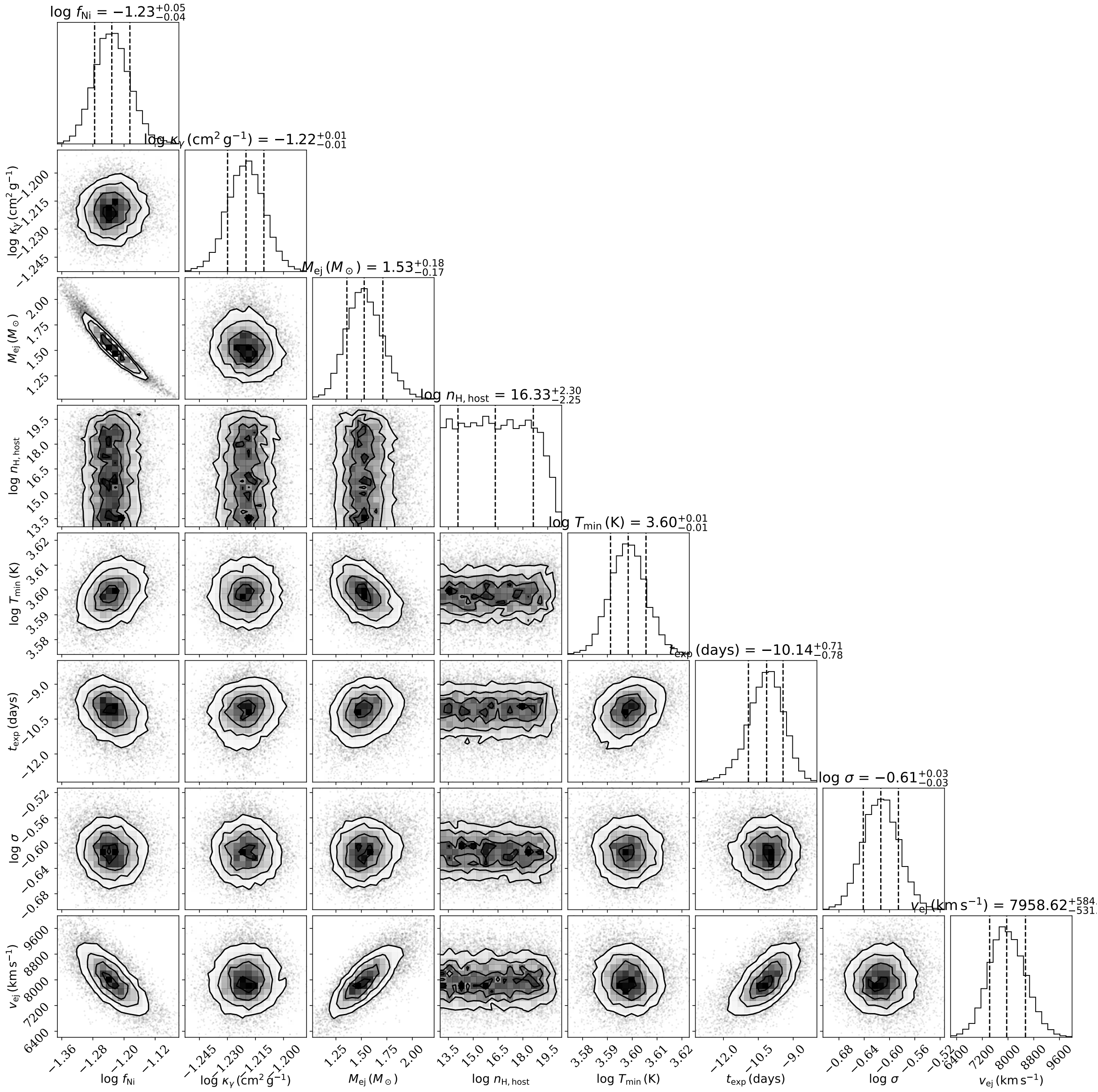

Figure 21. The 1D and 2D posterior distributions of the *default* ^{56}Ni model parameters in MOSFiT used for SN 2021mxx. The median and 1σ confidence intervals are marked to indicate the best-fit values of important physical parameters such as nickel fraction $f_{\rm Ni}$, ejecta mass $M_{\rm ej}$, k, k_γ, $t_{\rm exp}$, etc.

ORCID iDs

Mulchand Kurre https://orcid.org/0009-0000-4028-1263
K. R. Sahu https://orcid.org/0009-0001-3331-6883
N. K. Chakradhari https://orcid.org/0009-0007-8332-2812
D. K. Sahu https://orcid.org/0000-0002-6688-0800
Rishabh Singh Teja https://orcid.org/0000-0002-0525-0872
G. C. Anupama https://orcid.org/0000-0003-3533-7183
Mridweeka Singh https://orcid.org/0000-0001-6706-2749
Anirban Dutta https://orcid.org/0000-0002-7708-3831
Anjasha Gangopadhyay https://orcid.org/0000-0002-3884-5637

References

Albareti, F. D., Allende Prieto, C., Almeida, A., et al. 2017, ApJS, 233, 25
Arnett, D. 1996, Supernovae and Nucleosynthesis: An Investigation of the History of Matter from the Big Bang to the Present (Princeton (Princeton Univ. Press)
Arnett, W. D. 1982, ApJ, 253, 785
Asplund, M., Amarsi, A. M., & Grevesse, N. 2021, A&A, 653, A141
Astropy Collaboration, Price-Whelan, A. M., Lim, P. L., et al. 2022, ApJ, 935, 167
Astropy Collaboration, Price-Whelan, A. M., Sipőcz, B. M., et al. 2018, AJ, 156, 123
Astropy Collaboration, Robitaille, T. P., Tollerud, E. J., et al. 2013, A&A, 558, A33
Barna, B., Pereira, T., Taubenberger, S., et al. 2021, MNRAS, 506, 415
Bellm, E. C., Kulkarni, S. R., Graham, M. J., et al. 2019, PASP, 131, 018002
Berger, E., Kulkarni, S. R., & Chevalier, R. A. 2002, ApJL, 577, L5
Bersten, M. C., Benvenuto, O. G., Folatelli, G., et al. 2014, AJ, 148, 68
Bostroem, K. A., Valenti, S., Horesh, A., et al. 2019, MNRAS, 485, 5120
Bottinelli, L., Durand, N., Fouque, P., et al. 1993, A&AS, 102, 57
Bufano, F., Pian, E., Sollerman, J., et al. 2012, ApJ, 753, 67
Burke, J., Hiramatsu, D., Howell, D. A., McCully, C., & Pellegrino, C. 2020, TNSCR, 2020-241, 1
Cano, Z. 2013, MNRAS, 434, 1098
Cardelli, J. A., Clayton, G. C., & Mathis, J. S. 1989, ApJ, 345, 245
Chatzopoulos, E., Wheeler, J. C., & Vinko, J. 2012, ApJ, 746, 121
Chen, J., Wang, X., Ganeshalingam, M., et al. 2014, ApJ, 790, 120

Chugai, N. N. 2000, AstL, 26, 797
Clocchiatti, A., Wheeler, J. C., Brotherton, M. S., et al. 1996, ApJ, 462, 462
Corsi, A., Ofek, E. O., Frail, D. A., et al. 2011, ApJ, 741, 76
Das, K. K., Kasliwal, M. M., Sollerman, J., et al. 2024, ApJ, 972, 91
Davis, K. W., Taggart, K., Tinyanont, S., et al. 2023, MNRAS, 523, 2530
Dutta, A., Sahu, D. K., Anupama, G. C., et al. 2022, ApJ, 925, 217
Eldridge, J. J., Fraser, M., Maund, J. R., & Smartt, S. J. 2015, MNRAS, 446, 2689
Eldridge, J. J., Fraser, M., Smartt, S. J., Maund, J. R., & Crockett, R. M. 2013, MNRAS, 436, 774
Elmhamdi, A., Danziger, I. J., Cappellaro, E., et al. 2004, A&A, 426, 963
Filippenko, A. V., Porter, A. C., & Sargent, W. L. W. 1990, AJ, 100, 1575
Filippenko, A. V., & Sargent, W. L. W. 1985, Natur, 316, 407
Foley, R. J., Papenkova, M. S., Swift, B. J., et al. 2003, PASP, 115, 1220
Foley, R. J., Smith, N., Ganeshalingam, M., et al. 2007, ApJL, 657, L105
Foreman-Mackey, D. 2016, JOSS, 1, 24
Foreman-Mackey, D., Hogg, D. W., Lang, D., & Goodman, J. 2013, PASP, 125, 306
Forster, F., Munoz-Arancibia, A., Bauer, F. E., et al. 2021, TNSTR, 2021-1752, 1
Fransson, C., & Chevalier, R. A. 1987, ApJL, 322, L15
Fransson, C., & Chevalier, R. A. 1989, ApJ, 343, 323
Fraser, M., Stritzinger, M. D., Brennan, S. J., et al. 2021, arXiv:2108.07278
Freedman, W. L., Madore, B. F., Gibson, B. K., et al. 2001, ApJ, 553, 47
Fremling, C., Sollerman, J., Taddia, F., et al. 2016, A&A, 593, A68
Frey, L. H., Fryer, C. L., & Young, P. A. 2013, ApJL, 773, L7
Gal-Yam, A., Bruch, R., Schulze, S., et al. 2022, Natur, 601, 201
Galama, T. J., Vreeswijk, P. M., van Paradijs, J., et al. 1998, Natur, 395, 670
Gangopadhyay, A., Misra, K., Sahu, D. K., et al. 2020, MNRAS, 497, 3770
Ganss, R., Pledger, J. L., Sansom, A. E., et al. 2025, MNRAS, 543, 2374
Gkini, A., Lunnan, R., Schulze, S., et al. 2024, A&A, 685, A20
Guillochon, J., Nicholl, M., Villar, V. A., et al. 2018, ApJS, 236, 6
Harkness, R. P., & Wheeler, J. C. 1990, in Classification of 1217 Supernovae, ed. A. G. Petschek (Springer), 1, doi:10.1007/978-1-4612-3286-5_1
Hjorth, J., Sollerman, J., Møller, P., et al. 2003, Natur, 423, 847
Hunter, D. J., Valenti, S., Kotak, R., et al. 2009, A&A, 508, 371
Hunter, J. D. 2007, CSE, 9, 90
Iwamoto, K., Mazzali, P. A., Nomoto, K., et al. 1998, Natur, 395, 672
Jerkstrand, A., Ergon, M., Smartt, S. J., et al. 2015, A&A, 573, A12
Karamehmetoglu, E., Sollerman, J., Taddia, F., et al. 2023, A&A, 678, A87
Kasliwal, M. M., Kulkarni, S. R., Gal-Yam, A., et al. 2012, ApJ, 755, 161
Kerzendorf, W. E., & Sim, S. A. 2014, MNRAS, 440, 387
Kuncarayakti, H., Anderson, J. P., Galbany, L., et al. 2018, A&A, 613, A35
Kuncarayakti, H., Maeda, K., Bersten, M. C., et al. 2015, A&A, 579, A95
Kwok, L. A., Williamson, M., Jha, S. W., et al. 2022, ApJ, 937, 40
Landolt, A. U. 2009, AJ, 137, 4186
Limongi, M., & Chieffi, A. 2003, ApJ, 592, 404
Liu, Y.-Q., Modjaz, M., & Bianco, F. B. 2017, ApJ, 845, 85
Liu, Y.-Q., Modjaz, M., Bianco, F. B., & Graur, O. 2016, ApJ, 827, 90
Lyman, J. D., Bersier, D., James, P. A., et al. 2016, MNRAS, 457, 328
Maeda, K., Nomoto, K., Mazzali, P. A., & Deng, J. 2006, ApJ, 640, 854
Maeda, K., Tanaka, M., Nomoto, K., et al. 2007, ApJ, 666, 1069
Malesani, D., Tagliaferri, G., Chincarini, G., et al. 2004, ApJL, 609, L5
Masci, F. J., Laher, R. R., Rusholme, B., et al. 2019, PASP, 131, 018003
Masci, F. J., Laher, R. R., Rusholme, B., et al. 2023, arXiv:2305.16279
Matheson, T., Filippenko, A. V., Li, W., Leonard, D. C., & Shields, J. C. 2001, AJ, 121, 1648
Mazzali, P. A., Maurer, I., Valenti, S., Kotak, R., & Hunter, D. 2010, MNRAS, 408, 87
Mazzali, P. A., Sullivan, M., Pian, E., Greiner, J., & Kann, D. A. 2016, MNRAS, 458, 3455
Milisavljevic, D., Margutti, R., Parrent, J. T., et al. 2015, ApJ, 799, 51
Moore, T., Gillanders, J. H., Nicholl, M., et al. 2025, ApJL, 980, L44
Mould, J. R., Huchra, J. P., Freedman, W. L., et al. 2000, ApJ, 529, 786
Nadyozhin, D. K. 1994, ApJS, 92, 527
Nicholl, M. 2018, RNAAS, 2, 230
Nicholl, M., Smartt, S. J., Jerkstrand, A., et al. 2014, MNRAS, 444, 2096
Nomoto, K., Hashimoto, M., Tsujimoto, T., et al. 1997, NuPhA, 616, 79
Nomoto, K., Tominaga, N., Umeda, H., Kobayashi, C., & Maeda, K. 2006, NuPhA, 777, 424
Osterbrock, D. E. 1989, Astrophysics of Gaseous Nebulae and Active Galactic Nuclei (Univ. Science Books)
Pandey, S. B., Anupama, G. C., Sagar, R., et al. 2003, MNRAS, 340, 375
Pastorello, A., Smartt, S. J., Mattila, S., et al. 2007, Natur, 447, 829
Pedregosa, F., Varoquaux, G., Gramfort, A., et al. 2011, Journal of Machine Learning Research, 12, 2825
Pellegrino, C., Hiramatsu, D., Burke, J., et al. 2021, TNSCR, 2021-1794, 1
Pellegrino, C., Howell, D. A., Terreran, G., et al. 2022, ApJ, 938, 73
Perets, H. B., Gal-Yam, A., Mazzali, P. A., et al. 2010, Natur, 465, 322
Perley, D. A., Sollerman, J., Schulze, S., et al. 2022, ApJ, 927, 180
Pettini, M., & Pagel, B. E. J. 2004, MNRAS, 348, L59
Pian, E., Mazzali, P. A., Masetti, N., et al. 2006, Natur, 442, 1011
Prabhu, T. P. 2000, BASI, 28, 233
Prentice, S. J., Ashall, C., Mazzali, P. A., et al. 2018, MNRAS, 478, 4162
Prentice, S. J., Mazzali, P. A., Pian, E., et al. 2016, MNRAS, 458, 2973
Rauscher, T., Heger, A., Hoffman, R. D., & Woosley, S. E. 2002, ApJ, 576, 323
Richmond, M. W., van Dyk, S. D., Ho, W., et al. 1996, AJ, 111, 327
Sahu, D. K., Anupama, G. C., Chakradhari, N. K., et al. 2018, MNRAS, 475, 2591
Sahu, D. K., Tanaka, M., Anupama, G. C., Gurugubelli, U. K., & Nomoto, K. 2009, ApJ, 697, 676
Sauer, D. N., Mazzali, P. A., Deng, J., et al. 2006, MNRAS, 369, 1939
Schlafly, E. F., & Finkbeiner, D. P. 2011, ApJ, 737, 103
Shivvers, I., Modjaz, M., Zheng, W., et al. 2017, PASP, 129, 054201
Singh, M., Misra, K., Valenti, S., et al. 2021, ApJ, 909, 100
Singh, M., Sahu, D. K., Barna, B., et al. 2024, ApJ, 965, 73
Smartt, S. J. 2009, ARA&A, 47, 63
Smith, K. W., Smartt, S. J., Young, D. R., et al. 2020, PASP, 132, 085002
Smith, N., Foley, R. J., & Filippenko, A. V. 2008, ApJ, 680, 568
Smith, N., Li, W., Filippenko, A. V., & Chornock, R. 2011, MNRAS, 412, 1522
Speagle, J. S. 2020, MNRAS, 493, 3132
Srivastav, S., Moore, T., Nicholl, M., et al. 2023, ApJL, 956, L34
Stanek, K. Z., Matheson, T., Garnavich, P. M., et al. 2003, ApJL, 591, L17
Stritzinger, M., Mazzali, P., Phillips, M. M., et al. 2009, ApJ, 696, 713
Stritzinger, M. D., Taddia, F., Burns, C. R., et al. 2018, A&A, 609, A135
Taddia, F., Sollerman, J., Fremling, C., et al. 2019, A&A, 621, A71
Taddia, F., Stritzinger, M. D., Bersten, M., et al. 2018, A&A, 609, A136
Taubenberger, S. 2017, in Handbook of Supernovae, ed. A. W. Alsabti & P. Murdin (Springer), 317, doi:10.1007/978-3-319-21846-5_37
Taubenberger, S., Pastorello, A., Mazzali, P. A., et al. 2006, MNRAS, 371, 1459
Tody, D. 1993, ASPC, 52, 173
Tonry, J., Denneau, L., Heinze, A., et al. 2020, TNSTR, 2020-206, 1
Tonry, J. L., Denneau, L., Heinze, A. N., et al. 2018, PASP, 130, 064505
Toy, V. L., Cenko, S. B., Silverman, J. M., et al. 2016, ApJ, 818, 79
Uomoto, A. 1986, ApJL, 310, L35
Valenti, S., Benetti, S., Cappellaro, E., et al. 2008, MNRAS, 383, 1485
van der Walt, S., Colbert, S. C., & Varoquaux, G. 2011, CSE, 13, 22
Vartanyan, D., Laplace, E., Renzo, M., et al. 2021, ApJL, 916, L5
Virtanen, P., Gommers, R., Oliphant, T. E., et al. 2020, NatMe, 17, 261
Vogl, C., Sim, S. A., Noebauer, U. M., Kerzendorf, W. E., & Hillebrandt, W. 2019, A&A, 621, A29
Vreeswijk, P. M., Savaglio, S., Gal-Yam, A., et al. 2014, ApJ, 797, 24
Watanabe, S. 2010, Journal of Machine Learning Research, 11, 3571
Wheeler, J. C., & Harkness, R. P. 1986, ASIC, 180, 45
Williamson, M., Kerzendorf, W., & Modjaz, M. 2021, ApJ, 908, 150
Williamson, M., Vogl, C., Modjaz, M., et al. 2023, ApJL, 944, L49
Xiang, D., Wang, X., Mo, J., et al. 2019, ApJ, 871, 176
Yamanaka, M., Nakaoka, T., Tanaka, M., et al. 2017, ApJ, 837, 1
Yan, L., Quimby, R., Ofek, E., et al. 2015, ApJ, 814, 108
Yaron, O., & Gal-Yam, A. 2012, PASP, 124, 668
Yoon, S.-C. 2015, PASA, 32, e015
Yoon, S. C., Woosley, S. E., & Langer, N. 2010, ApJ, 725, 940
Zhang, J., Wang, X., Vinkó, J., et al. 2018, ApJ, 863, 109